Investigations of Size and Strain Rate Influences on Fracture Surfaces of Smooth Tensile Specimens of Austenitic X6CrNiNb 18 10 (1.4550) and Ferritic-Baintic Steels 20MnMoNi5 5 (1.6310)

E. Materna-Morris, P. Graf, H. Zimmermann, T. Malmberg

Institut für Materialforschung
Institut für Reaktorsicherheit
Programm Nukleare Sicherheitsforschung

Forschungszentrum Karlsruhe

in der Helmholtz-Gemeinschaft

Wissenschaftliche Berichte

FZKA 6525

Investigations of Size and Strain Rate Influences on Fracture Surfaces of Smooth Tensile Specimens of Austenitic X6CrNiNb 18 10 (1.4550) and Ferritic-Baintic Steels 20MnMoNi5 5 (1.6310)

E. Materna-Morris, P. Graf, H. Zimmermann and T. Malmberg

Institut für Materialforschung

Institut für Reaktorsicherheit

Programm Nukleare Sicherheitsforschung

Forschungszentrum Karlsruhe GmbH, Karlsruhe

2002

Abstract

To investigate the influence of different strain rates and sample sizes, tensile specimens of the reactor steels X6CrNiNb18 10 (1.4550) and 20MnMoNi5 5 (1.6310) were fabricated and tested at room temperature. The structures and fractures of these samples were examined to detect such influences on the fracture behaviour of these materials.

The tensile samples of the austenitic steel X6CrNiNb18 10 with a diameter of 3 mm in the uniform section were tested at strain rates of 10^{-3}, 10^{-1}, 10, and 200 s^{-1}. In these series, the loss of ductility due to the deformation velocity could be shown. This behaviour was recognizable in the lower necking of the fractures and the tendency to larger dimple diameters in the fracture surfaces. These specimens were compared with another series of tensile tests using geometrically similar specimens of 30 mm diameter. The strain rates during the tensile tests were 10^{-3} and 150 s^{-1}. With increasing strain rate and diameter of the gauge length, a decrease of the necking could be determined together with increasing dimple diameter.

The tensile samples of the steel 20MnMoNi5 5 with 3 and 30 mm diameter were tested again at 10^{-3} and 200 s-1. Under all test conditions, the samples were broken in a ductile mode; either cup and cone, shear or milling cutter type of fractures were observed. As a particular result of the size effect, the 30 mm samples were broken at the low strain rate with a milling cutter type fracture, while the small samples broke with a cup and cone fracture. In the necking and the formation of the voids in the fracture surface, such an influence of the test parameters could not be observed as could be seen in the austenitic steel.

Untersuchungen zum Einfluß der Probengrößen und Dehngeschwindigkeiten auf die Bruchoberflächen von gleichförmigen Zugproben aus austenitischem X6CrNiNb18 10 (1.4550) und ferritisch-bainitischem Stahl 20MnMoNi5 5 (1.6310)

Inhalt

Um die Einflüsse von unterschiedlichen Dehnungsgeschwindigkeiten und Probengrößen zu untersuchen, wurden aus den Reaktorstählen X6CrNiNb18 10 (1.4550) und 20MnMoNi5 5 (1.6310) Zugproben hergestellt und bei Raumtemperatur geprüft. Das Gefüge und die Brüche dieser Proben wurden begutachtet, um solche Einflüsse auf das Bruchverhalten der Materialien zu erkennen.

Die Zugversuche des austenitischen Stahls X6CrNiNb18 10 (1.4550), mit einem Meßlängendurchmesser von 3 mm, wurden bei Dehngeschwindigkeiten von 10^{-3}, 10^{-1}, 10 und 200 s^{-1} geprüft. Bei dieser Serie konnte die Abnahme der Zähigkeit mit Zunahme der Dehngeschwindigkeit beobachtet werden. Dieses Verhalten war anhand der geringeren Brucheinschnürung und der Tendenz zu größeren Wabendurchmessern in den Bruchoberflächen erkennbar. Diese Proben wurden mit einer weiteren Serie mit geometrisch ähnlichen Zugproben von 30 mm Meßlängendurchmesser verglichen. Die Dehngeschwindigkeiten während der Zugversuche waren 10^{-3} und 150 s^{-1}. Hier wurde mit zunehmender Dehngeschwindigkeit und Messlängendurchmesser eine Abnahme der Brucheinschnürung beobachtet, verbunden mit der Zunahme der Wabendurchmesser.

Die Zugproben aus dem Stahl 20MnMoNi5 5 mit 3 und 30 mm Messlängendurchmesser wurden ebenfalls bei Dehngeschwindigkeiten von 10^{-3} und 200 s^{-1} geprüft. Unter allen Prüfkonditionen brachen die Proben in einem zähen, entweder in einem Trichter-, Scher- oder Fräserbruch. Als einen besonderen Probengrößeneinfluss konnte festgestellt werden, dass die 30 mm-$\varnothing$-Proben bei niedriger Dehngeschwindigkeit als Fräserbruch brachen und die kleinen Proben mit 3 mm Durchmesser als Trichterbruch. Bei der Brucheinschnürung und den Wabenformen in der Bruchoberfläche konnte solch ein Einfluss durch die Versuchsparameter nicht gefunden werden, wie es beim austenitischen Stahl beobachtet wurde.

Contents:

1. Objectives

Within the framework of the EU-project REVISA (Reactor Vessel Integrity in Severe Accidents), Nuclear Fission Safety Programme Project FI4S-CT96-0024, a subtask was formulated: Size Effects. Since the beginning of the materials testing, these investigations have been aimed at clarifying the following question: Are the data of the mechanical test of a small sample transferable to a larger component ? One primary aspect of this task is to analyse the mechanical properties together with the formation of material fracture when changing the size of geometrically similar tensile specimen s. Such an expected size effect is investigated in tensile tests and quantified by the material behaviour before and after tensile tests based on data of the structure and the fracture surfaces of the tested samples. A literature survey regarding size effects in smooth tensile specimens is given in reference [1]. In addition, the influence of slow and fast deformation velocities on the tensile data was to be studied.

In the present paper, two materials were provided for the experimental work; an austenitic steel X6CrNiNb18 10 and a ferritic-bainitic pressure vessel steel 20MnMoNi5 5. The tensile samples of the austenitic steel were manufactured with gauge length diameters of 3 and 30 mm, respectively. As all samples, the 3 mm-samples were tested at RT (Room Temperature) up to the fracture with strain rates of 10^{-3}, 10^{-1}, 10, and 200 s^{-1}. In these series, ductility (area reduction) was found to be reduced by an increasing strain rate in the tensile tests. To obtain further information on the fracture surfaces, however, the fracture mode and different features of the fracture surfaces were to be determined, described, and quantified. The data of these samples were to be compared with the features and data of samples of 30 mm diameter, which were tested at strain rates of 10^{-3} and 150 s^{-1}.

The broken tensile samples of the steel 20MnMoNi5 5 were investigated in the same way. The samples with diameters of 3 and 30 mm were tested up to fracture at slow strain rates of 10^{-3} s^{-1} and very fast rates of 200 or 150 s^{-1}, respectively.

In this report, data are summarised with regard to the material structures, grain sizes, grain size distribution, hardness, and the fracture formations, like necking, area of normal stress fracture, average dimple sizes, and dimple size distributions. The results are discussed taking into account the original structure of the material and the mechanical properties.

This collection of data is one part of this project, in which other European partners and laboratories are involved with design, mechanical tests, and theoretical modelling.

2.   Experimental Procedure

2.1   Materials

The reactor materials tested were an austenitic and a ferritic-bainitic steel. The austenitic steel X6CrNiNb18 10 (DIN 1.4550) is the actual material of the upper internal structure of the reactor pressure vessel. The chemical composition is given in Table 1, as indicated by the supplier in the acceptance sheet. The material, taken from a single heat, was delivered in plates (70 x 300 x 1000 mm), after forging, solution annealing, and quenching.

The chemical composition of the ferritic-bainitic steel 20MnMoNi5 5 (DIN 1.6310) for the re-actor pressure vessel is shown in Table 2. The given values are in accordance with the ma-terial certificate. Heat treatment after forging consisted of an austenitisation at 900 °C, water quenching, heat treatment at 730 °C, and air cooling inside the furnace. The material, a sin-gle heat, was provided in the form of a set of plates (70 x 500 x 1000 mm).

The different samples were cut and fabricated. Detailed cutting planes were provided, such that the specimens of different type and size were distributed over the plates, the larger (30 mm diameter) specimens positioned at the mid-planes and the small ones also over the thickness (70 mm) of the plates. Samples also included standard tensile and Charpy impact specimens of one size to be used for quality assurance and homogeneity assessment. All specimens were oriented parallel to the long edges of the plates. Of course, each specimen was properly marked to allow an identification of its origin (material, plate, position).

For manufacturing reasons, the small specimens (e.g. 3 mm diameter tensile specimens) were grouped together in small sections of the plates. This generally implied that the smallest specimens were not positioned in the neighbourhood of the largest ones. The quality assur-ance and homogeneity assessment program was carried out and reported by Krompholz et. al. [2, 3]. Positional influences were noted, which must be accounted for in the interpretation of the results; see Refs. [4, 5].

2.2. Mechanical Tests

The smooth cylindrical tensile specimens were tested at JRC (Joint Research Centre), Ispra, Italy. In the technical note no. I.99.127 of G. Solomos et.al. [6], the mechanical program is summarised. Tensile samples of 3 and 30 mm diameter were tested at RT, 400, and 600 °C. Both quasi-static and dynamic tensile tests were carried out at strain rates between 10^{-3} and 150 or 200 s^{-1}.

The tensile specimens used by JRC are designed according to the needs in dynamic testing: The wave propagation phenomena required a short uniform section ($L_0/D_0 \sim 1.7$, L_0 and D_0, length and diameter of uniform section) and a smooth transition section, Fig. 0. This form is fairly different from standard tensile specimens ($L_0/D_0 \sim 5 - 6$). It is noted that this latter type of specimens was used by Krompholz et.el. [7] for size effect studies of the ferritic-bainitic steel under quasi-static condition. For a discussion of these results, see Refs. [4, 5].
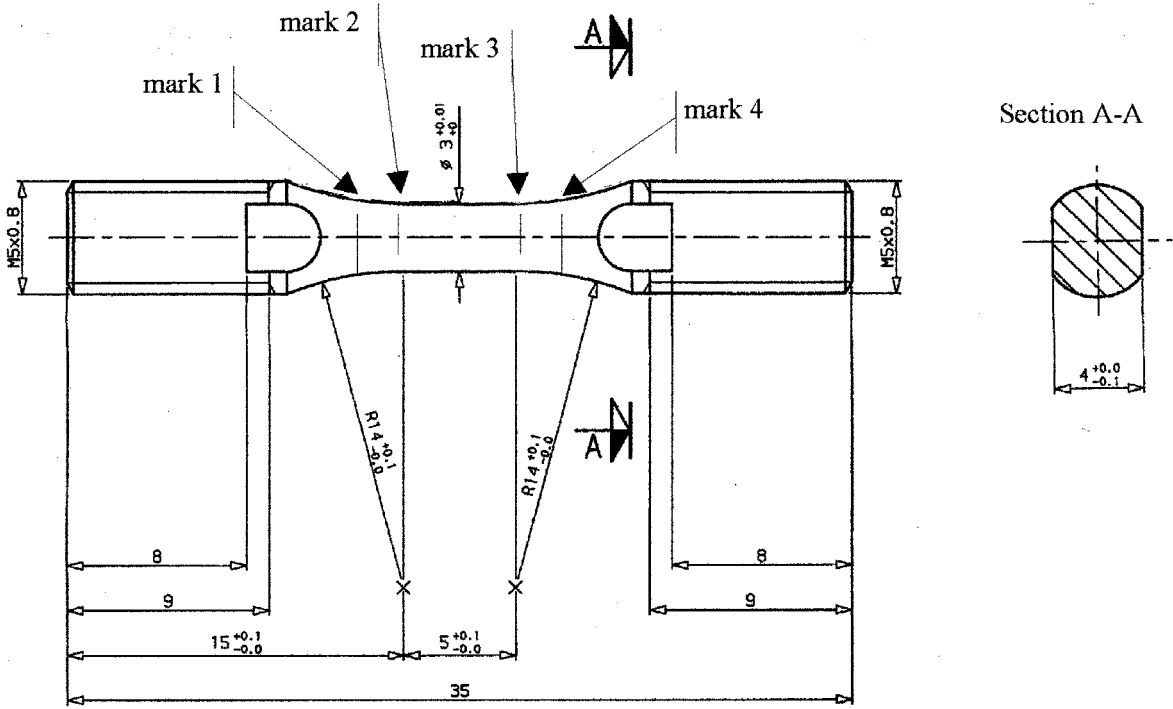
Fig. 0: Geometry of the 3 mm cylindrical tensile specimen.

Within the extensive JRC program, a selected number of samples tested at RT was post-examined in order to determine the microstructure and fracture modes. A first investigation series of small austenitic tensile samples (3 mm diameter) was compiled to show the effects of the four different strain rates only; Table 3 (from Ref. [6]). The second series was to compare the influence of the strain rates and the size effect of the tensile samples of the austenitic, Table 4, and the ferritic material, Table 5 (from Ref. [4]).

2.3. Investigation Methods

All broken tensile samples were examined visually and documented by macroscopic photographs. The heads of the fractures were cut off and studied by means of SEM (Scanning Electron Microscopy), the microscope being equipped with an EDX unit (Energy Dispersive X-Ray Analysis) to analyse the chemical components of the materials and inclusions. The structures of the materials were investigated using metallographic cuts. The hardness was measured by the Vickers method; HV10 and HV1. All hardness values and the grain sizes were determined in the heads of the samples, where the material was not deformed. The quantitative data of the structure and fracture surfaces were determined by a picture-analysing system: SIS Version 3.1. The dimple areas were measured, classified, and the ECD (Equivalent Circle Diameter) was calculated to determine the average diameter. The necking of the fractures was measured by SEM pictures. The relative value of the normal stress fracture area N was determined as the necking Z with Ao (initial cross-section area), A (area of the cross-section after fracture), and A_N (area of the normal stress fracture):

Definition of necking or reduction of area Z:

$$Z[\%] = \frac{Ao - A}{Ao} 100\%$$

definition of normal stress fracture area N:

$$N[\%] = \frac{Ao - A_N}{Ao} 100\%$$

The roughness of some fracture surfaces, in the normal stress fracture only, was measured in the middle-length cuts by means of R_z and R_{max}; EN ISO 4287 and DIN 4768. R_{max} was the maximum distance between the highest and lowest altitude. The R_{z5} value was determined along the profile of the normal stress fracture by 5 segments:

$$R_{z5} = \sum_{i=1}^{5} Z_i \frac{1}{5}$$

3. Results

3.1 Influence of Strain Rate on the Structure and Fracture Formation of Small Austenitic Steel Specimens (X6CrNiNb18 10)

The first investigation series were carried out with the tensile samples of the austenitic steel X6CrNiNb18 10 only; Table 3. All samples had the same diameter of 3 mm, but they were tested at different strain rates; $\dot{\varepsilon}$ = 10^{-3}, 10^{-1}, 10, and 200 s^{-1}. Two results obtained by Solomos et. al. [6] should be mentioned first: The ultimate stress R_m of the small specimen tested at RT increased slightly with increasing strain, which is a common phenomenon, however, the area reduction at fracture decreased (Tab. 4). The question arose whether this reduction in ductility was some-how correlated with other properties of the fractures.

Metallographic cuts were prepared as middle-length cuts through the fractures and the threaded head of all samples. The typical austenitic grain structure with the twin planes was observed. In the selected specimens, a variation of grain sizes was noticed (Figs. 1, 2). The grain sizes (ECD) of the samples were found to be 20 µm or, in another case, up to 100 µm. Note that the corresponding specimens (Tab. 3) came from the same plate and section, but from different positions along the thickness direction. The hardness was measured, too, and varied between 137HV10 and 154, Table 6. In this Table, some tensile data obtained by Solomos et. al. [6] are entered as well.

In all samples, a high density of line structures of inclusions, primary carbides, and δ-ferrite was observed with the average distance of these lines being up to 85 µm (Figs. 3 a, b). The δ-ferrite contained 5 wt.% more of the Cr component than the matrix.

Fracture investigations were carried out on the tested samples H1A05, H1A11, H1A15, and H1A20 (Fig. 4). All samples had a ductile fracture mode. Fracture appearance, however, changed from cup and cone fracture (H1A05) at the low strain rate of 10^{-3} s^{-1} to fracture formation with a high proportion of shear fracture (H1A20) at the high strain rate of 200 s^{-1}.

In the microstructure of the fractures, inclusions and primary carbides NbC were found (Fig.5). Chemical analysis showed that the inclusions consisted of Mn-O, MnS, Al_2O_3, and Ca-Si oxide particles. Usually, primary carbides were found in the same area as the inclusions (Fig. 6). Some of the inclusions could be seen on the specimen surface (Fig. 7). δ-ferrite could not be identified on the fracture surfaces. The determined roughness showed an increase due to the strain rate (Tab. 6). H1A20 was not measured, because the normal stress fracture in the metallographic cut was too small and the sample was broken more in a shear fracture.

Special attention was given to the areas of normal stress fractures. To obtain some quantitative data from the fractures, the areas of the normal stress fractures were measured for the

different strain rates. The normal stress fracture area N was correlated to the round flat area at the bottom of the cup and cone fracture. From Fig. 8, it was evident that the area reduction Z of the four selected 3 mm-diameter specimens decreased monotonically with increasing strain rate, a qualitative finding that is in agreement with numerous measurements of Solomos reported in [6]. However, the relative normal stress fracture area N was almost independent of the strain rate. Observing the definition of Z and N,

$$\frac{A_N}{A} = \frac{1-N}{1-Z}$$

is obtained, which is the fraction of the normal stress fracture area relative to the final deformed neck area. From the above empirical findings, it can be concluded that this normal stress area fraction decreases with increasing strain rate. This result is well demonstrated in Figs. 14 and 15.

Further data were derived from the dimples in the centres of the fractures (Figs. 9, 10). The areas of the dimples were measured and divided into 20 classes between 0 and 200 μm^2 to show the frequency distributions. Most dimples were dimples with small areas of the first class between 0 and 10 μm^2 (Fig. 11). The amount of small dimples (10 μm^2) was found to be reduced (Fig. 11) with increasing strain rate, whereas the average dimple diameter (ECD) increased considerably from 4.0 to 6.8 μm.

X6CrNiNb18 10

H1A05 Gauge length $\varnothing$ = 3 mm, $\acute{\epsilon}$ = 2 x 10^{-3} s^{-1} Average dimple $\varnothing$ = 4.0 μm	H1A11 Gauge length $\varnothing$ 3 mm, $\acute{\epsilon}$ = 10 s^{-1} Average dimple $\varnothing$ = 6.8 μm
H1A15 Gauge length $\varnothing$ 3 mm, $\acute{\epsilon}$ = 1 x 10^{-1} s^{-1} Average dimple $\varnothing$ = 4.9 μm	H1A20 Gauge length $\varnothing$ 3 mm, $\acute{\epsilon}$ = 200 s^{-1} Average dimple $\varnothing$ = 6.5 μm

3.2. Structure and Fracture Formation at Different Sample Size and Strain Rates

Both materials, the austenitic and the ferritic-bainitic vessel steel, were compared. The two sample sizes (3 and 30 mm diameter) discussed here were tested in quasi-static tensile tests at a strain rate of 10^{-3} s^{-1} and in dynamic tests at 200 s^{-1}.

Austenitic Steel, X6CrNiNb18 10:

It should be noted that the small specimens (3 mm diameter) were produced from sections in the centre of a long edge, but from various positions over the thickness (70 mm) of the plates. The large specimens (30 mm diameter), however, were centred at the mid-plane.

Because of budget restrictions of JRC, the homogeneity assessment was restricted to chemical analysis, hardness tests, and some metallographic investigations; see Krompholz [3]. Thus, the positional influence on the mechanical properties is not known.

Some of the tensile test results obtained by Solomos et. al. [6] are collected in Tab. 4. Obviously, the ultimate stress R_m is considerably larger for the small specimens under quasi-static conditions than for the large specimens. Following the discussion by Malmberg et al. [4], it appears that this is a pseudo-size effect induced by a positional effect. The decrease of the reduction of area Z, however, likely was a true effect.

All large tested and fractured tensile samples were documented macroscopically (Figs. 12, 13). The fractures had the typical ductile cup and cone formation (Figs. 14, 15). At the strain rate of 200 s^{-1}, no influence of the inclusions on the sample surface with a formation of shear fracture could be noted, as observed in the small samples (Fig. 4).

Unlike the previous investigations, the structures of the large tensile samples exhibited a homogeneous distribution of the austenitic grain size between 50 – 60 µm. This appeared to be plausible, because all large specimens had been taken from the mid-planes of the plates. The line structure of the δ-ferrite, the inclusions, and primary carbides were the same as observed in the small tensile samples.

The average dimple diameter decreased with increasing specimen size both for the quasi-static and the dynamic strain rate. The size distribution, however, did not show any clear trend (Figs. 16 – 19):

X6CrNiNb18 10

H1A05	H1A20
Gauge length $\varnothing$ = 3 mm, $\acute{\epsilon}$ = 1 x 10^{-3} s^{-1}	Gauge length $\varnothing$ 3 mm, $\acute{\epsilon}$ = 200 s^{-1}
Average dimple $\varnothing$ = 4.0 µm	Average dimple $\varnothing$ = 6.5 µm
H3A01	H3A12
Gauge length $\varnothing$ 30 mm, $\acute{\epsilon}$ = 1 x 10^{-3} s^{-1}	Gauge length $\varnothing$ 30 mm, $\acute{\epsilon}$ = 150 s^{-1}
Average dimple $\varnothing$ = 2,2 µm	Average dimple $\varnothing$ = 4.8 µm

Table 7 in the Appendix gives the grain sizes, hardness values, and roughness together with the known tensile strengths.

The tensile tests of sample H1A13, H1A14 and H1A15 were repeated in H 1A29, H1A31 and H1A31, but these samples were not available for investigations [6].

Ferritic-Bainitic Steel, 20MnMoNb5 5:

The second type of material was the ferritic-bainitic reactor pressure vessel steel. This material had a very fine structure with a grain diameter of 30 – 50 µm of the primary austenitic grain (Fig. 20). A high density of carbides was distributed in the material. Wieland et al. [8, 9] analysed them as M_3C. By light microscopy, dark segregation bands could be seen parallel to the forging direction, in which the carbides were coarser and had a higher density. There was an enrichment of carbon and the micro hardness was higher than in the matrix:

Matrix: HV1 = 153

Segregation band: HV1 = 213

The bright matrix next to the segregation bands had a lower hardness, an effect of carbon segregation. These areas contained less carbon. The average distance of these bands was determined to be in the range of 200 µm. The final microstructure was adjusted by the deformation of the structure due to forging and the final heat treatment. The average hardness, measured with a higher load, was found to be in the range of 200 HV10.

The tensile samples of 3 and 30 mm in diameter were tested at RT with strain rates of 10^{-3} and 200 s^{-1}. The corresponding tensile test data obtained by Solomos et al. [6] are presented in Table 5. The ultimate stress R_m is consistently larger for the small specimens, no matter whether small or large strain rates are applied. An extensive supplementary homogeneity assessment [10] for the ferritic-bainitic vessel steel and further analysis have demonstrated that this observation is a pseudo-size effect due to the inhomogeneity of the plates. It was shown in [4] that small and large specimens, both taken from an area as close as possible to mid-plane of the plates, do not differ in the ultimate stress under quasi-static strain rates, whereas the area reduction Z decreases with size. All fractures (Figs. 21 - 24) were ductile formations, but the morphology was different. The small samples had cup and cone fracture surfaces. The large samples of 30 mm diameter also exhibited a cup and cone fracture at the fast strain rate (150 s^{-1}), but the slow strain rate caused a milling cutter type fracture with a small area of normal stress fracture in the centre (Fig. 23). As can be seen in Figs. 23 and 24, the first half of the fractures was cut after the tensile test for first investigations. SEM of the middle-length cut through the fracture provided further information: Near the fracture surfaces, cracks could be observed in the segregation bands, which were perpendicular to the main stress (Figs. 25, 26). Further crack initiators were the MnS inclusions with their strong development of cavities.

The fractographic microstructure was investigated, too. The fracture surface revealed a very fine dimple formation due to the fine grain structure and the body-centered cubic matrix. Only five to seven large dimples could be found in the centres of the fractures (10 – 30 µm $\varnothing$). In these very deep dimples, it was difficult to analyse the inclusions. In a few cases, however,

MnS could be found. The statistical distribution of the dimples was determined in a much higher magnification (5000 x) than in the austenitic steel (500 x) (Fig. 27). The statistical distribution of the dimple sizes shows a quasi-exponential decaying frequency with increasing dimple size for both specimen sizes and strain rates (Fig. 28). From Fig. 28, it is also evident that an increase in size or strain rate somewhat reduces the frequency of the first dimple size classes. The average dimple diameter varied moderately from 0.9 to 1.15 µm. Thus, the dimple diameter is almost independent of the strain rate and specimen size.

20MnMoNi5 5

H1013 Gauge length $\varnothing$ = 3 mm, $\acute{\varepsilon}$ = 2 x 10^{-3} s^{-1} Average dimple $\varnothing$ = 0.9 µm	H1003 Gauge length $\varnothing$ 3 mm, $\acute{\varepsilon}$ = 200 s^{-1} Average dimple $\varnothing$ = 1.0 µm
H3030 Gauge length $\varnothing$ 30 mm, $\acute{\varepsilon}$ = 1 x 10-3 s^{-1} Average dimple $\varnothing$ = 1.0 µm	H3001 Gauge length $\varnothing$ 30 mm, $\acute{\varepsilon}$ = 150 s^{-1} Average dimple $\varnothing$ = 1.15 µm

The reduction of area at fracture Z decreases with increasing specimen size (Fig. 29), especially at the quasi-static strain rate of 10^{-3} s^{-1}, whereas differences are small at the dynamic rate of 150 s^{-1}. The normal stress area reduction N appears to be independent of the specimen size and strain rate.

All data determined with regard to the structures and fractures of the investigated samples are listed in Table 8.

Roughness of the fracture surfaces:

Further information on the ductility would be the depth of the dimples, but there was no opportunity to measure the third dimension. Only the qualitative impressions of the SEM images were obtained. Another first impression was gained from the middle-length cuts through the fractures with an estimation of the fracture roughness: The roughness of all investigated samples rises with higher strain rates and from small to large samples; see Tables 6-8.

4. Conclusions

Tensile tests of two steels used in reactor technology, the austenitic steel X6CrNiNb18 10 used for upper internal structures and the ferritic-bainitic reactor pressure vessel steel 20MnMoNi5 5, were performed by IRC (Solomos et al. [6]) to determine the influence of the specimen size and strain rate on the tensile characteristics. Subsequently, the fractured specimens were investigated with respect to their metallographic structure and their fracture morphology.

The austenitic steel X6CrNiNb18 10 (1.4550) is a transformation-free steel and the grain structure is adjusted by the content of carbides (NbC etc.) and recrystallisation treatment. The structural investigations showed that the material was not homogeneous. In metallographic cuts of the different tensile samples, different grain sizes were determined; this is related to the origin of the specimens in terms of the position within the plate. The hardness values confirmed the tendency that the material with smaller grains has a higher hardness ($\varnothing$ = 30 µm and HV10 = 154) than the material with coarser grains ($\varnothing$ = 100 µm and HV10 = 137). Apparently, the grain size and the hardness do not have such a distinctive influence on the tensile strength (Tab. 6).

The differences in the material structure were induced by forging and cold working of the plate material. Material with a high deformation produced a fine grain during the recrystallisation heat treatment. This occurs on or near the surface of the plate during the fabrication. The small tensile samples ($\varnothing$ 3 mm) were made from a single section within the plate, but from different depths. This effect was not observed in the larger samples ($\varnothing$ 30 mm). These samples were very large compared to the plate dimension of 70 mm thickness and could be taken only from the mid-plane of the plate.

In all samples a line structure of inclusions, δ-ferrite, and primary carbides could be seen. The observed δ-ferrite is a soft phase from the melt with a very low carbon content of about 0.02 wt.%. No influence on the fracture behaviour could be noticed.

During the first series with this material ($\varnothing$ 3 mm) only, was the influence of different strain rates (10^{-3}, 10^{-1}, 10, 200 s^{-1}) investigated. A change from the fracture cup and cone at the lowest strain rate to an increased contribution of shear fracture at the highest strain rate was found. This behaviour is due to the higher deformation velocity and the deformation behaviour of the material around the inclusions and precipitates. During the slow deformation, the material had time to glide slowly and formed the necking and the typical cup and cone fracture with a flat normal stress fracture surface in the centre, which was subjected to a 3-

dimensional stress state that was normal to the largest tensile stress component. When the crack approached the surface of the tensile sample, the 3-dimensional state of stress changed to a 2-dimesional state, and the formation of the shear lips began. The inclusions initiated the formation of very large dimples at the bottom of the cup. They did not influence the formation of the shear lips at slow strain rates.

At the high strain rate, fracture started in the centre of the sample, too. Probably at the same time, formation of shear fracture occurred. Shear formation started from the surface of the sample in the 2-dimensional stress state. It is known that pure shear fractures are initiated at the surfaces of the tensile samples when there are severe defects, such as corrosion or small cracks. In our example, the defects were inclusions in the sample surface.

Comparison between the small and large tensile samples did not reveal any essential influence. All large samples were broken in the cup and cone mode. The areas of the normal stress fracture were nearly the same. The influence of the sample size became visible in the development of the shear lips. The shear lips were more developed in the large samples.

In the microstructure of the fractures, the average dimple sizes increased in the areas due to the strain rates. The formation of larger and more flat dimples can be explained by the shorter time to glide, develop, and form the dimple walls.

These results of the metallographic investigations of the austenitic steel showed the difficulty to determine a clear size effect in these series. Material inhomogeneity has an adverse effect on the interpretation of the tensile data.

The ferritic-bainitic steel 20MnMoNi5 5 (1.6310) is a hardenable steel. The usual heat treatment consists of an austenitisation, quenching, and tempering. The austenitisation treatment, quenching and the distribution of the primary carbides are important for the grain size of the material. There was no obvious change in the grain sizes between all samples. Especially remarkable was the line structure of segregation along the forging direction.

In these test series, the large and small tensile samples were compared after the quasi-static and dynamic tensile test. All these samples fractured in a ductile mode and, as shown by Solomos et al. [6] and Malmberg et al. [4], the area reduction of fracture Z decreased when the size increased. This macroscopic behaviour can be compared with the austenitic material with one exception. A milling cutter type fracture was observed in the large samples at the slow strain rate, whereas the fast strain rate induced a cup and cone fracture. On the contrary, the small specimens always fractured with cup and cone fracture, whether tested at a slow or fast strain rate. Thus, there is a remarkable interplay of size and strain rate, which

produces a size – strain rate dependence of the fracture morphology. On the other hand, the dimple diameters showed hardly any influence of sample size or strain rate.

The formation of the milling cutter type or rosette star-type fracture is typical for tensile samples fabricated from hot-worked plates with a line structure of segregation or inclusions [11, 12]. A splitting radial from the centre of the fracture can be seen. The relatively uniform distribution in different directions of the splitting shows a nearly uniform rolling work of the plate. At the low strain rate ($1x10^{-3}$ s^{-1}), the first crack started in the centre of the neck of the material. There was a 3-dimensional state of stress and the crack started normal to maximum stress, the tensile stress. But due to the line structure in the sample with relatively brittle carbon and precipitation segregation, the material had not enough strength in circumferential direction. The material splitted into longitudinally oriented separations. In these thin separations, the 2-dimensional state of stress prevailed and the material sheared off at 45°. It is very remarkable to see this fracture formation only at the slow strain rate in the large sample, but not in the ten times smaller ones. Possibly, this size influence can be given a probabilistic explanation in the sense that the probability of the presence of a weak segregation is higher in the larger volume. The fact that under the fast strain rate the milling cutter type fracture did not occur may be an indication of time-dependent processes being involved in the production of this type of fracture. This could indicate why the segregation structures does not have such a paramount importance at the high strain rate.

Comparison of the austenitic (X6CrNiNb18 10) and ferritic-bainitic (20MnMoNi5 5) steels in terms of fracture behaviour shows that the macroscopic deformation is nearly the same, except for the formation of the milling cutter type fracture of the ferritic-bainitic steel at low strain rates and large sample diameters.

The different structures of these materials are responsible for the fracture microstructure. Dimple formation in the austenitic steel is much more influenced by the sample sizes and strain rates than in the ferritic-bainitic material. This behaviour is due to the different crystallographic structures of the materials; the austenitic steel has a face-centered cubic structure, which has a much higher plasticity than the body-centred cubic structure of the ferritic-bainitic steel. On the other hand, dimple formation is also influenced by the inclusions and precipitates in the material. They act as initiators of dimples. In the austenitic steel there are much less inclusions and carbides than in the ferritic-bainitic steel. At slow strain rate, there can be formed larger and deeper dimples in the face-centered cubic matrix. With higher strain rates, the dimple diameter grows, as there is less time to form many deep dimples, and the reduction of the sample diameter decreases. These effects could not be observed in the fracture-microstructure of the ferritic-bainitic steel. There are so many carbides, they all represent

initiators of dimples. Thus, in the fractures of this material, only a minor increase in the dimple size due to sample size or strain rate was visible. Only in few cases large dimples develops around inclusions. In this ferritic-bainitic steel, more influence is observed by the crack formation in the carbide segregation of the matrix.

5. References

[1]   Malmberg T., Tragratis I., Eleftheriadis I., Aifantis E.C.: On the Gradient Plasticity Approach to Size Effects, Part I: Reviews. Forschungszentrum Karlsruhe Scientific Report FZKA 6321, March 2001.

[2]   Krompholz K., Kamber J. and Kalkhof D.: A preliminary study of material homogeneity for size effect investigations. PSI Bericht Nr. 99-03, June 1999, ISSN 1019-0643.

[3]   Krompholz K.: Quality assurance of the austenitic steel X6CrNiNb18 10 (1.4550), Paul Scherrer Institut, PSI-TM-49-98-07, Sept. 1998.

[4]   Malmberg T., Krompholz K., Solomos G. and Aifantis E.C.: Investigation on Size Effects in Ferritic and Austenitic Materials; Trans. 15th Int.Conf. on Structural Materials in Reactor Technology (SMiRT-15), Seoul, Korea, Aug. 15-20,1999, X-299-X-306.

[5]   Malmberg T., Krompholz K., Kalkhof D., Solomos G., Aifantis E.C.: Size Effects in Deformations and Fractures of a Ferritic Reactor Pressure Vessel Steel; Trans. 16th Int.Conf. on Structural Materials in Reactor Technology (SMiRT-16), Washington D.C., USA, Aug. 11-17, 2001, Division F, paper 1224.

[6]   Solomos G., Albertini C. and Labibes K.: Experimental Investigation of Strain Rate, Temperature and Size Effects in Nuclear Steels, Part I: The Smooth Cylindrical Specimens, Technical note no. I.99.127, JRC, July 1999.

[7]   Krompholz K., Kamber J., Groth E., Kalkhof D.: Size effect studies on smooth tensile specimens at room temperature and at 400 °C, PSI-Report No. 00-02, June 2000.

[8]   Wieland H.-J.: Mechanische Untersuchungen und elektronenmikroskopische Untersu-chungen des Einflusses der Neutronenstrahlung auf die Versprödung von Stählen in verschiedenen Gefügezuständen. Dissertation an der Rheinisch-Westfälischen Techni-schen Hochschule Aachen, Stuttgart 1986.

[9]   Wieland, H.-J., Klaar H.-J.: Flächengrößenanalyse von M_3C-Ausscheidungen mittels Kohlenstoffextraktionabdruck zur Kennzeichnung des Einflusses der Neutronenbe-strahlung auf das Gefüge des Reaktordruckbehälterstahls. Sonderbände der Prakt. Metallographie, Bd. 17, S. 287 – 297, 1985.

[10]   Malmberg T., Dolenzky B., Krompholz K.:Supplementary Evaluation of Material Homo-geneity in Six Plates of the Ferritic Steel 20 MnMoNi5 5, INV-REVISA (00)-P014, Dec. 2000.

[11]   Lange G.: Systematische Beurteilung technischer Schadensfälle. Deutsche Gesell-schaft für Metallkunde e.V., 1983, S. 82 – 85.

[12]   Van der Voort, G. F.: Visual Examination and Light Microscopy; in: Metals Handbook, Ninth Edition, Vol. 12, Fractography, ASM International, 1987, 91-165.

6. Appendix

Table 1: Chemical composition of steel X6CrNiNb18 10 in wt.%.

C	Si	Mn	P	S	Cr	Ni	Mo	Co	Nb	Nb/C
0.025	0.32	1.70	0.028	0.002	18.00	10.36	-	0.08	0.43	17.2

Table 2: Chemical composition of steel 20MnMoNi5 5 in wt.%.

C	Si	Mn	P	S	Cr	Ni	Mo	Co	Ta	Cu
0.2 – 0.23	0.28 – 0.33	1.30 – 1.21	0.009	0.002 – 0.005	0.11	0.65 – 0.71	0.44 – 0.47	0.01 – 0.02	0.005	0.030 – 0.036

N	V	Al	Sn
0.005	0.003 – 0.05	0.28	0.006

Table 3: Selection of tensile samples subjected to different strain rates at RT;
H1A = 3 mm Ø.

Specimen no.	Plate	Area	Strain rate [s^{-1}]	Test temperature
H1A05 x	1	A129	10^{-3}	RT
H1A06	1	A129	10^{-3}	RT
H1A07	1	A129	10^{-3}	RT
H1A09	1	A129	10	RT
H1A10	1	A129	10	RT
H1A11 x	2	A229	10	RT
H1A12	2	A229	10^{-1}	RT
H1A13	2	A229	10^{-1}	RT
H1A14	2	A229	10^{-1}	RT
H1A15 x	2	A229	10^{-1}	RT
H1A18	2	A229	200	RT
H1A19	2	A229	200	RT
H1A20 x	2	A229	200	RT

X: Microstructural and fractographic investigations

Table 4: Steel X6CrNiNb18 10: Tensile characteristics of specimens H1A = 3 mm Ø and H3A = 30 mm Ø.

Specimen no.	d_0 [mm]	Plate/ section	$\dot{\varepsilon}$ [s^{-1}]	R_m [MPa]	Z [%]
H1A05	3	A1/29	$1 \cdot 10^{-3}$	614	84
H1A06	3	A1/29	$1 \cdot 10^{-3}$	612	84
H1A07	3	A1/29	$1 \cdot 10^{-3}$	615	84
H3A01	30	A1/01	$1 \cdot 10^{-3}$	579	77
H3A02	30	A1/07	$1 \cdot 10^{-3}$	578	75
H3A03	30	A1/10	$1 \cdot 10^{-3}$	580	77
H1A18	3	A1/29	200	636	74
H1A19	3	A1/29	200	642	74
H1A20	3	A1/29	200	647	73
H3A09	30	A2/10	150	625	71
H3A10	30	A2/14	150	625	71
H3A11	30	A2/25	150	624	72
H3A12	30	A2/30	150	644	73

Table 5: Steel 20MnMoNi5 5: Tensile characteristics of specimens H10 = 3 mm Ø and H30 = 30 mm Ø.

Specimen no.	d_0 [mm]	Plate/ section	$\dot{\varepsilon}$ [s^{-1}]	R_{eH} [MPa]	R_{eL} [MPa]	R_m [MPa]	Z [%]
H1012	3	03/04	$2 \cdot 10^{-3}$	-	-	665	78
H1013	3	03/04	$2 \cdot 10^{-3}$	-	-	662	78
H1017	3	03/04	$2 \cdot 10^{-3}$	-	-	619	79
H3018	30	08/07	$1 \cdot 10^{-3}$	-	-	602	71
H3027	30	09/10	$1 \cdot 10^{-3}$	-	-	609	67
H3030	30	09/17	$1 \cdot 10^{-3}$	-	-	599	68
H1002	3	02/05	200	647	586	757	73
H1003	3	02/05	200	600	550	724	71
H1004	3	02/05	200	631	576	755	70
H3001	30	02/09	150	-	-	672	71
H3002	30	02/10	150	591	497	659	73
H3003	30	02/34	150	531	497	680	73
H3004	30	02/35	150	573	486	658	74

Table 6: Steel X6CrNiNb18 10: Structure data of the tensile samples tested at different strain rates.

Specimen no.	d_0 [mm]	Strain rate [s^{-1}]	R_m [N/mm^2]	Grain size $\varnothing$ [µm]	Hardness HV10	R_{Z5} [µm]	R_{max} [µm]	Dimple $\varnothing$ [µm]
H1A05 x	3	1×10^{-3}	614	80	147	39	75	4.0
H1A06	3	1×10^{-3}	612	70	154			
H1A07	3	1×10^{-3}	615	70	154			
H1A13	3	10^{-1}		60	153			
H1A14	3	10^{-1}		60	152			
H1A15 x	3	10^{-1}		40	145	51	108	4.9
H1A09	3	10	625	100	149			
H1A10	3	10	600	70	150			
H1A11 x	3	10	619	20	153	64	248	6.8
H1A18	3	200	636	80	145			
H1A19	3	200	644	100	137			
H1A20 x	3	200	647	70	151	-	-	6.5

X: Detailed microstructural and fractographic investigations

Table 7: Steel X6CrNiNb18 10: Structure data of the tensile samples with different sample sizes and tested at different strain rates.

Specimen no.	d_0 [mm]	Strain rate [s^{-1}]	R_m [N/mm^2]	Grain size $\varnothing$ [µm]	Hardness HV10	R_{Z5} [µm]	R_{max} [µm]	Dimple $\varnothing$[µm]
H1A05	3	1×10^{-3}	614	80	147	39	75	4.0
H1A06	3	1×10^{-3}	612	70	154			
H1A07	3	1×10^{-3}	615	70	154			
H3A01	30	1×10^{-3}	579	60	140	402	733	2.2
H3A02	30	1×10^{-3}	578	60	142			
H3A03	30	1×10^{-3}	580	60	142			
H1A18	3	200	636	80	145			
H1A19	3	200	642	100	137			
H1A20	3	200	647	70	151	-	-	6.5
H3A09	30	150	625	70	136			
H3A11	30	150	624	50	135			
H3A12	30	150	644	50	135	404	580	4.8

Table 8: Steel 20MnMoNi5 5: Structure data of the tensile samples with different sample sizes and tested at different strain rates.

Specimen no.	d_0 [mm]	Strain rate [s^{-1}]	R_m [N/mm^2]	Grain size Ø [µm]	Hardness HV10	R_{Z5}	R_{max}	Dimple Ø[µm]
H1012	3	2 x 10^{-3}	665		206	69	134	
H1013	3	2 x 10^{-3}	662	20	199	51	89	0.9
				-				
H3018	30	1 x 10^{-3}	602	50				
H3027	30	1 x 10^{-3}	609					
H3030	30	1 x 10^{-3}	599		196	712	1115	1.0
H1002	3	200	757		192	52	92	1.0
H1003	3	200	724		196			
H1004	3	200	755	20	197			
				-				
H3001	30	150	672	50	190	421	567	1.2
H3002	30	150	659		190			
H3003	30	150	680		134			
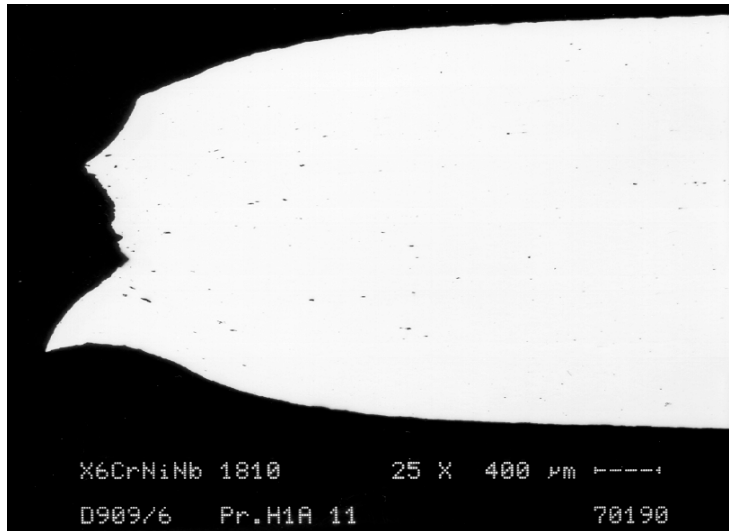
Middle length cut through the fracture (polished, 25x)
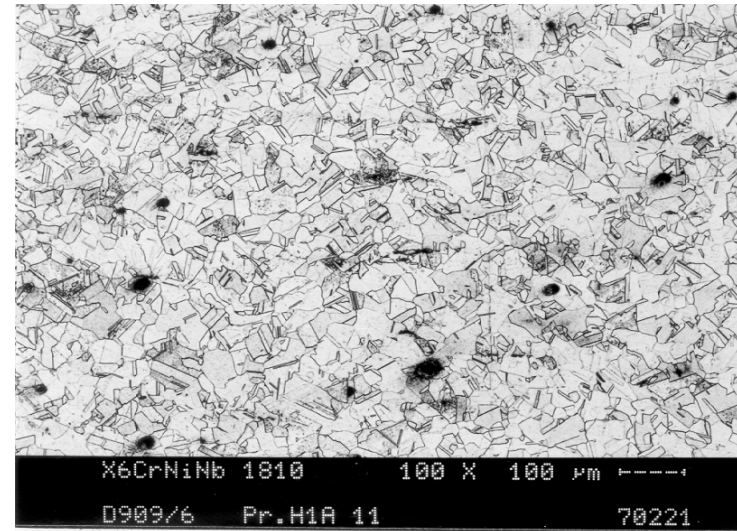
Grain formation in the sample head (etched, 100x)
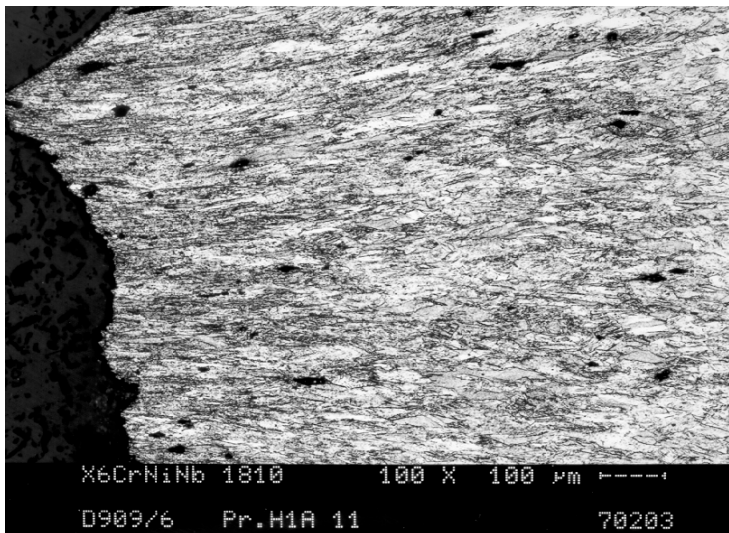
Grain formation of the fracture (etched, 100x)
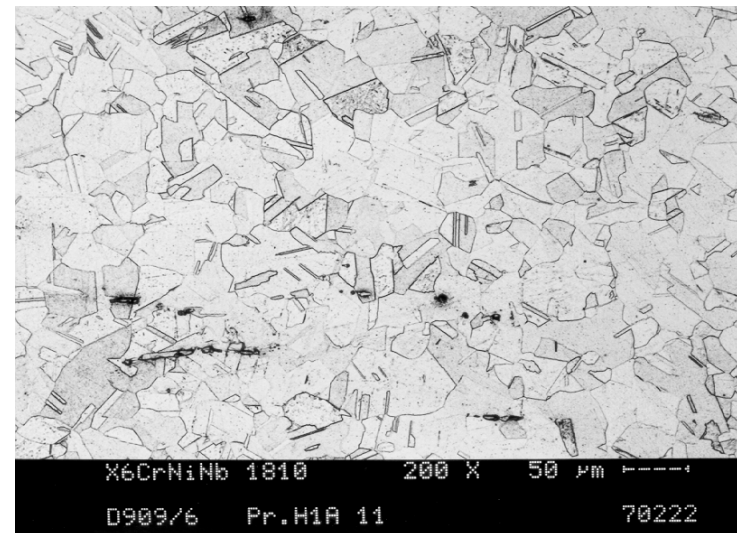
Grain formation in the sample head (etched, 200x)

Fig. 1: Metallographic cut of sample H1A11 with a small grain size.

Middle length cut through the fracture (polished, 25x)
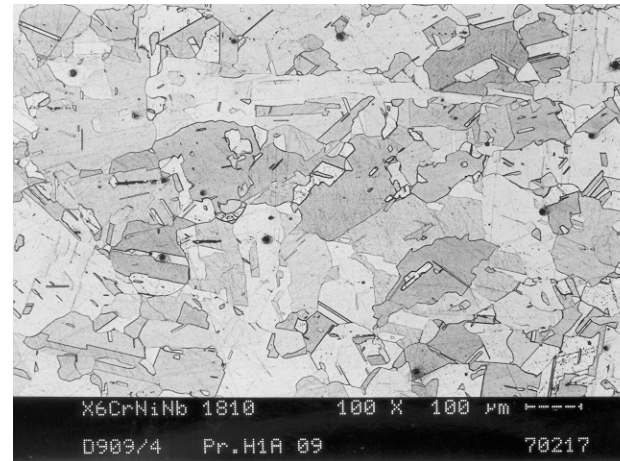
Grain formation in the sample head (etched, 100x)
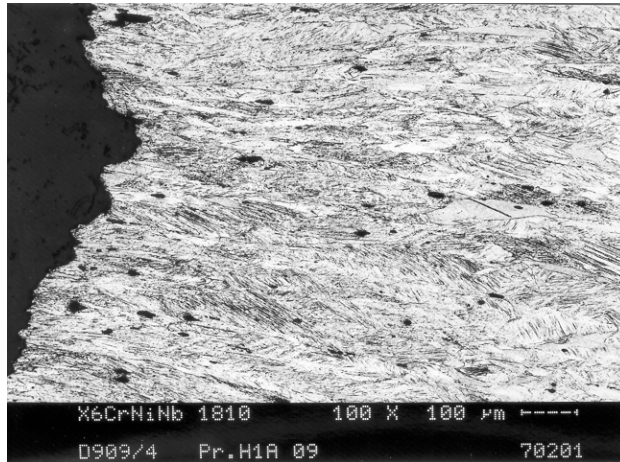
Grain formation of the fracture (etched, 100x)
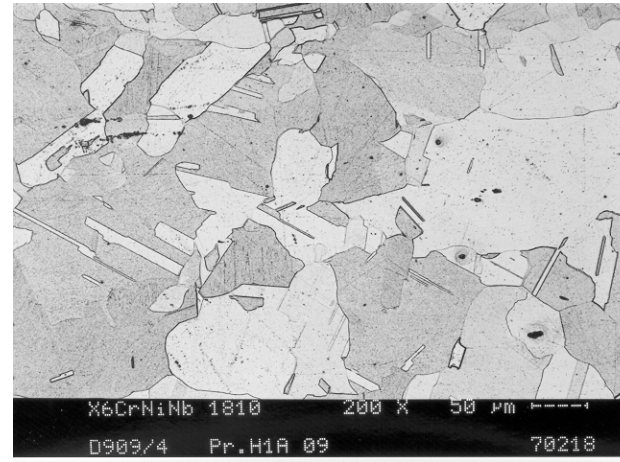
Grain formation in the sample head (etched, 200x)

Fig. 2: Metallographic cut of sample H1A19 with a large grain size.
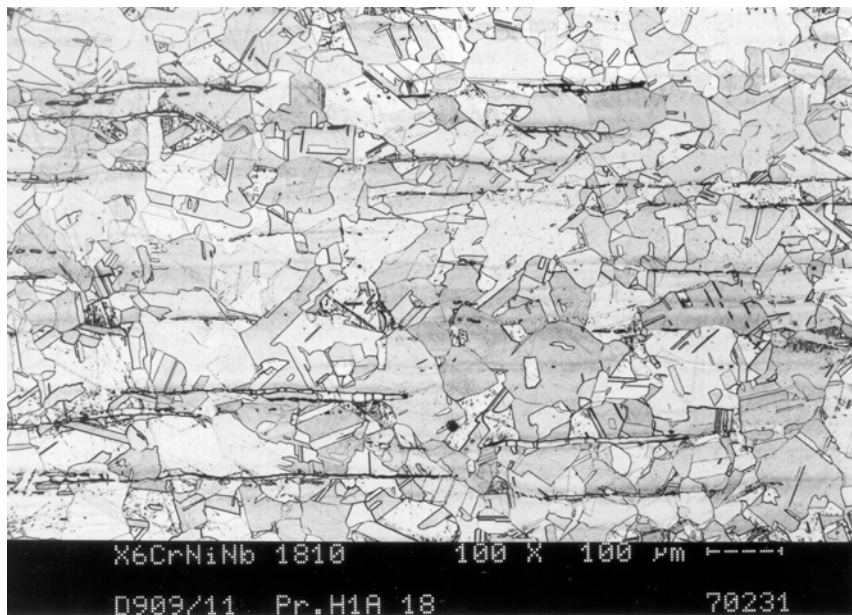
a) Overview of a high δ-ferrite density
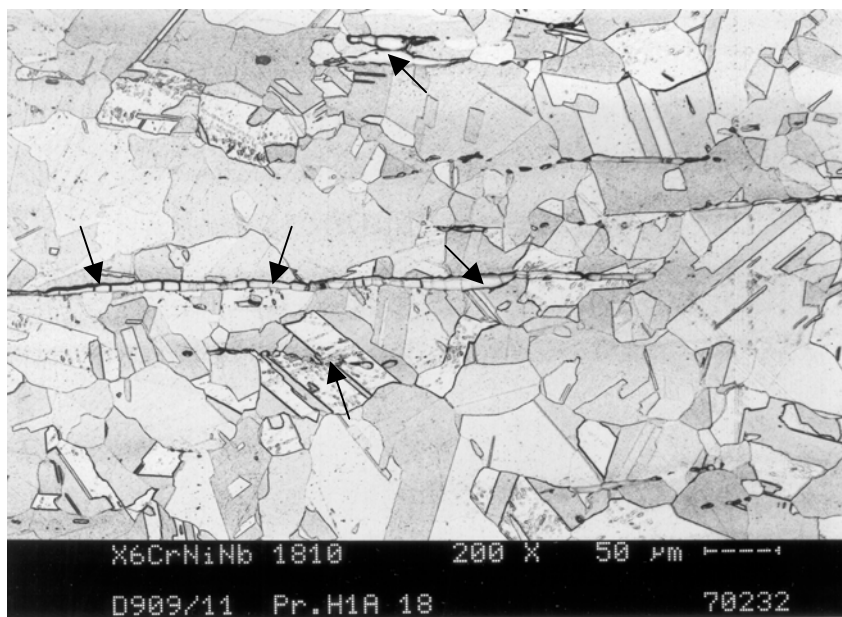
b) The lines with δ-ferrite are marked with arrows.

Fig. 3: δ-ferrite formation in sample H1A18.

21
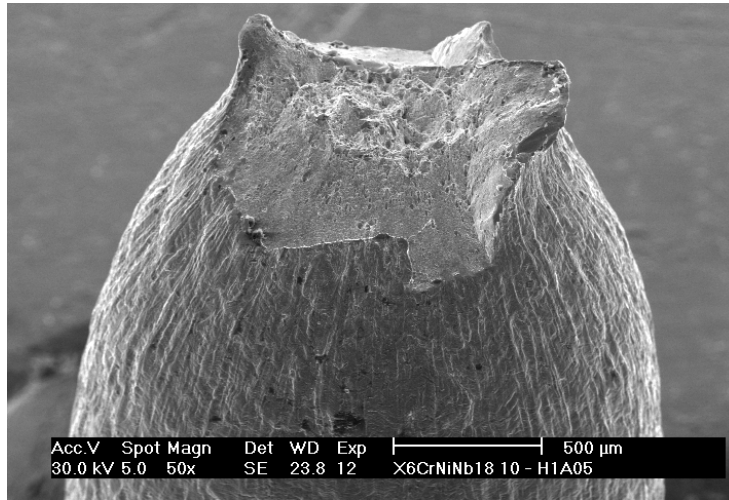
H1A05 ($\varnothing$ = 3 mm, $\acute{\epsilon}$ = 10^{-3} s^{-1})
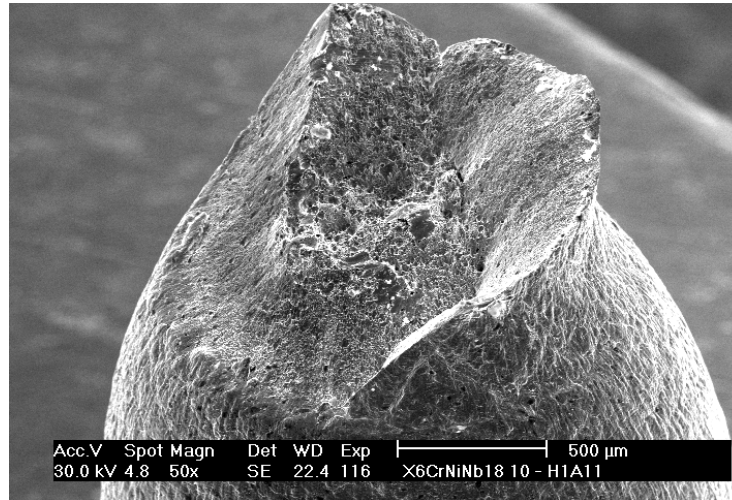
H1A11 ($\varnothing$ = 3 mm, $\acute{\epsilon}$ = 10 s^{-1})
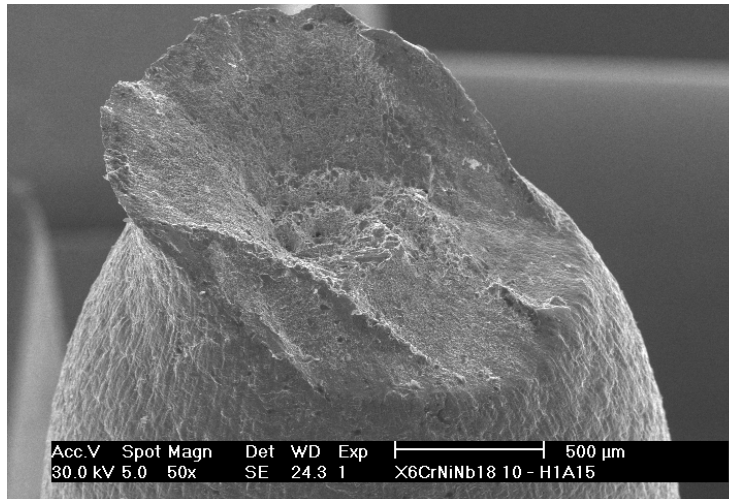
H1A15 ($\varnothing$ = 3 mm, $\acute{\epsilon}$ = 10^{-1} s^{-1})
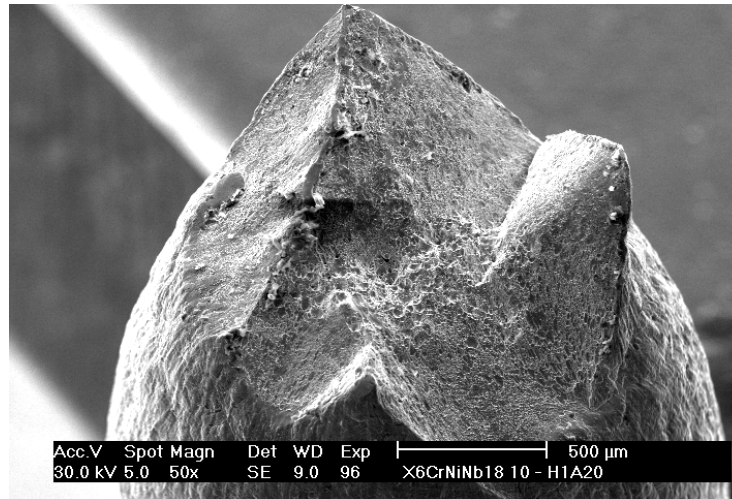
H1A20 ($\varnothing$ = 3 mm, $\acute{\epsilon}$ = 200 s^{-1})

Fig. 4: The fractures of the tensile samples tested at different strain rates.

22

Fracture overview, normal to the fracture surface.

| kV:30.0 | Tilt:0.00 | Tkoff:35.00 | Tkoff: | Res:132.30 | TC:40 |
| FS : 1754 | LSec : 15 | Prst:None | 14-Dec-98 | 17:42:23 | |
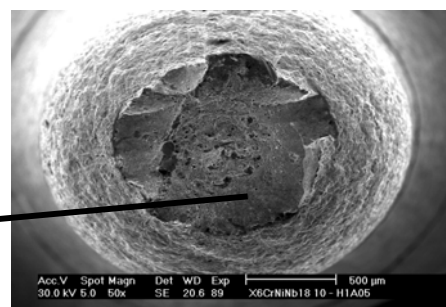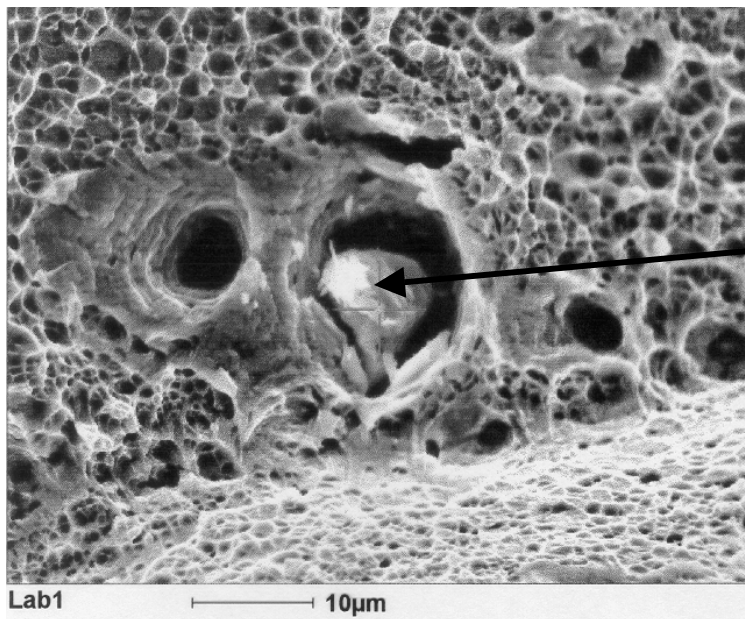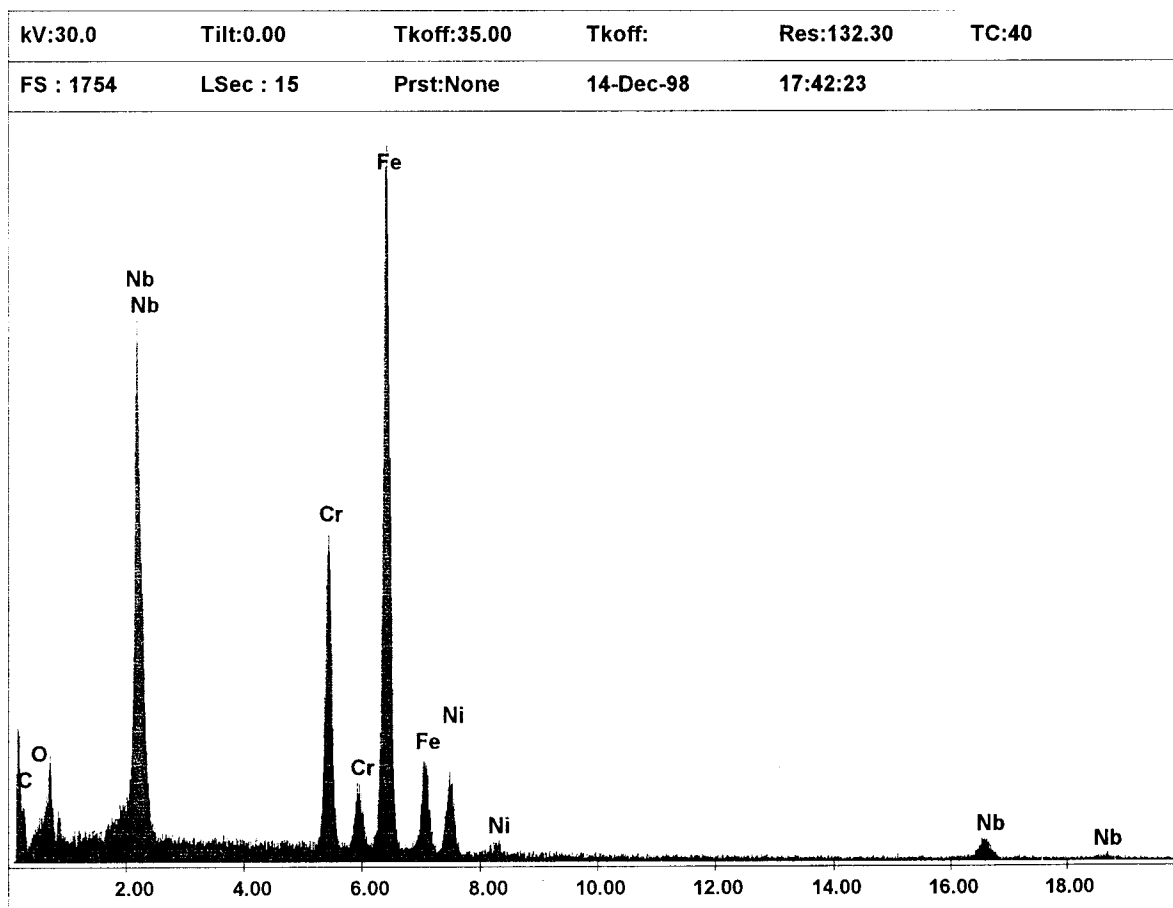
Fig. 5: EDS spectra of a primary carbide NbC in a large dimple of the fracture surface; sample H1A05.

Fracture overview, normal to the fracture surface.

| kV:30.0 | Tilt:0.00 | Tkoff:35.00 | Tkoff: | Res:132.30 | TC:40 |
| FS : 1252 | LSec : 90 | Prst:None | 14-Dec-98 | 17:11:58 | |
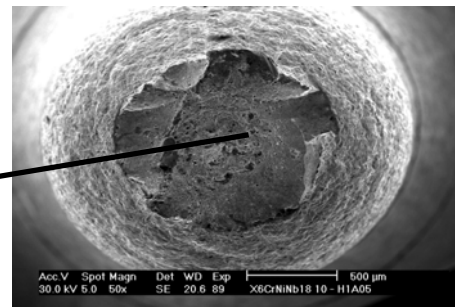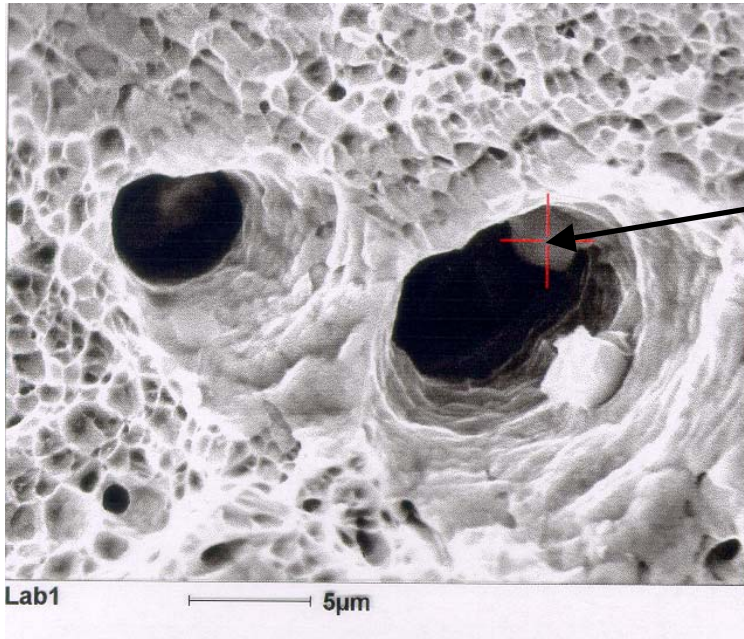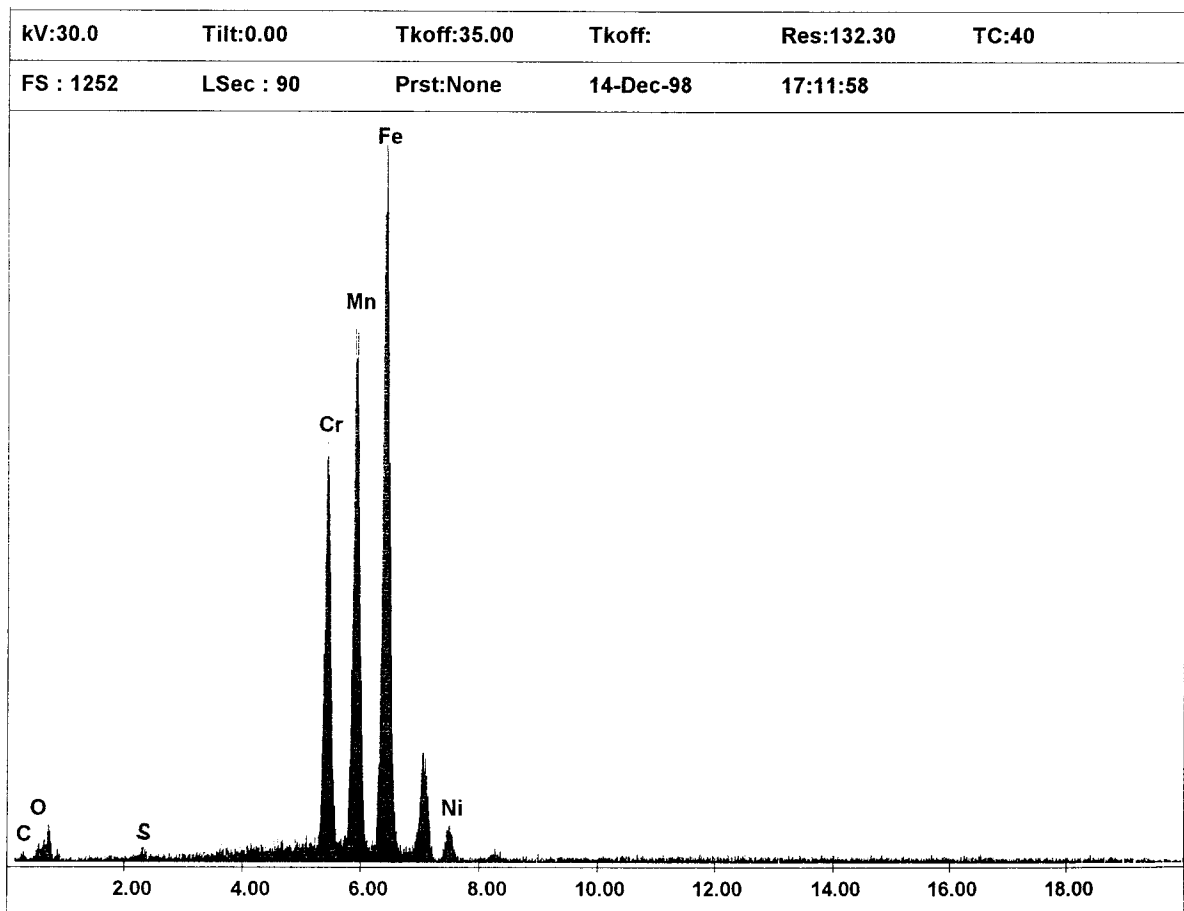
Fig. 6: EDS spectra of an Mn inclusion in a large dimple of the fracture surface; sample H1A05. The white particle in the same dimple is NbC.
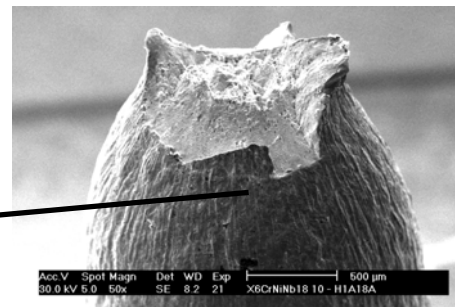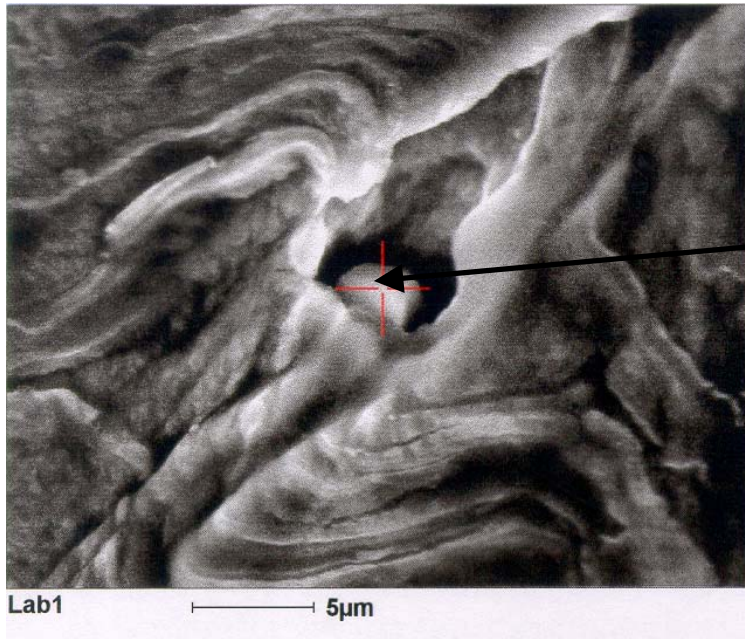
Side view of the fracture.
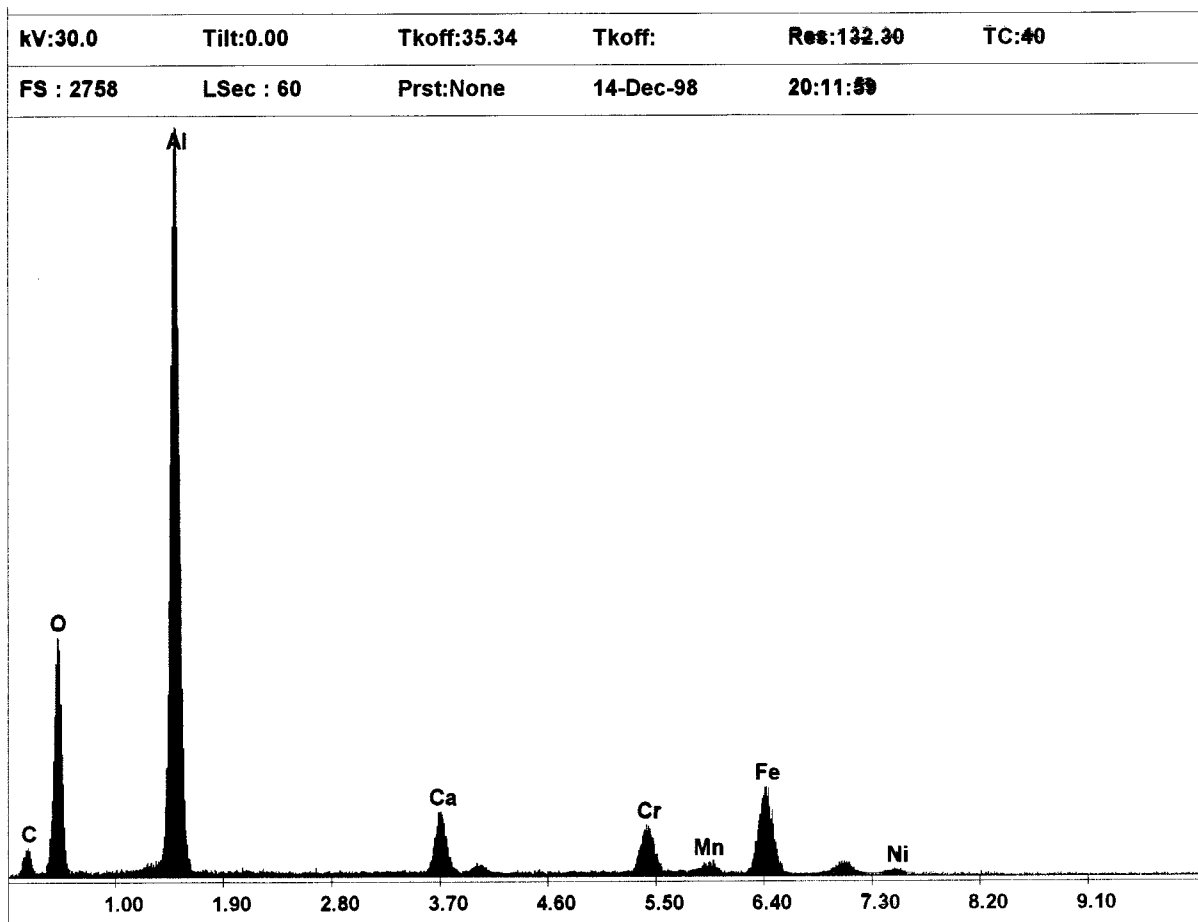
Fig. 7: EDS spectra of an Al_2O_3 inclusion in a dimple at the sample surface; sample H1A05.
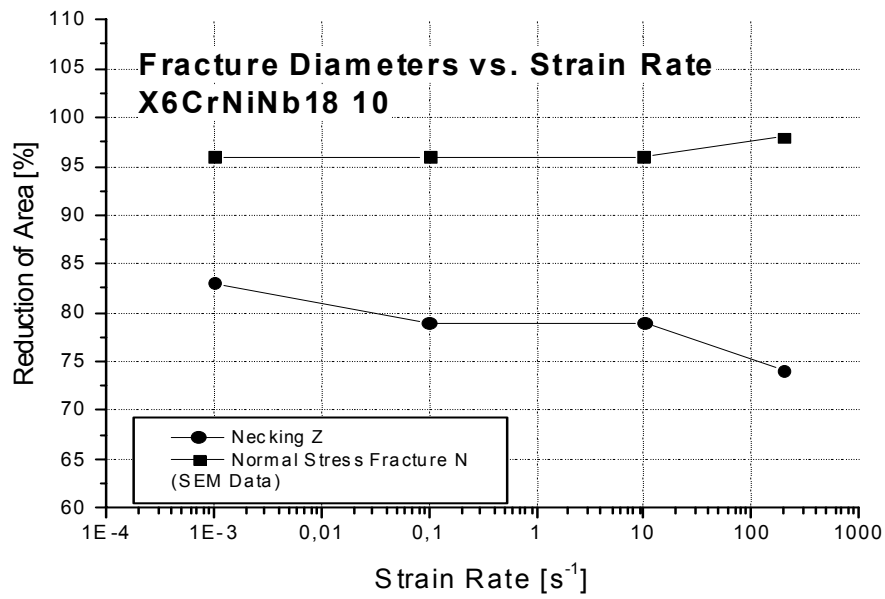
Fig. 8: Macroscopic fracture dimensions depending on the strain rates.
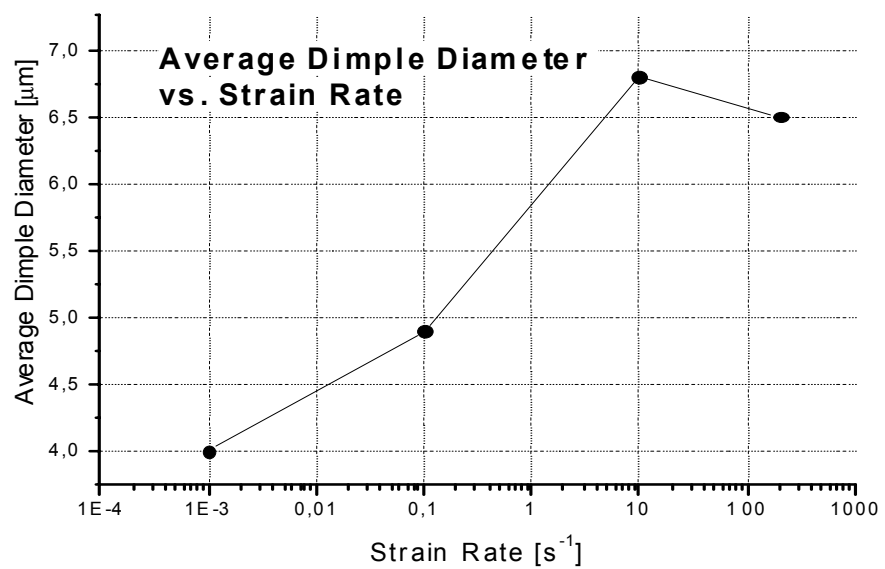
Fig. 9: Average dimple size depending on the strain rates.
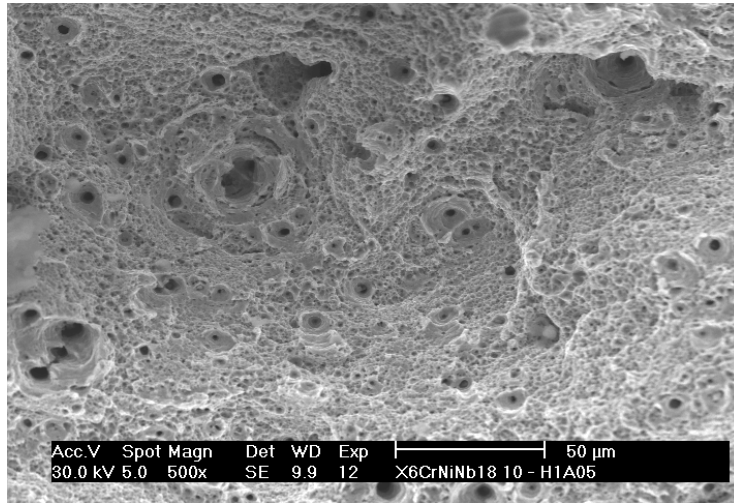
H1A05 ($\varnothing$ = 3 mm, $\acute{\varepsilon}$ = 10^{-3} s^{-1})
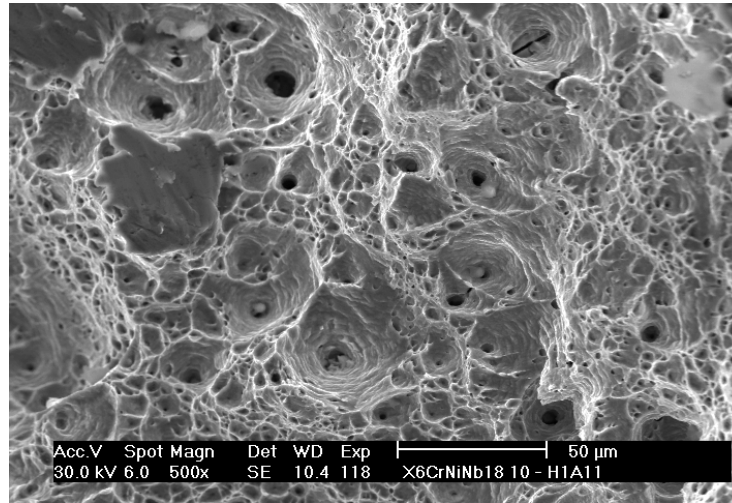
H1A11 ($\varnothing$ = 3 mm, $\acute{\varepsilon}$ = 10 s^{-1})
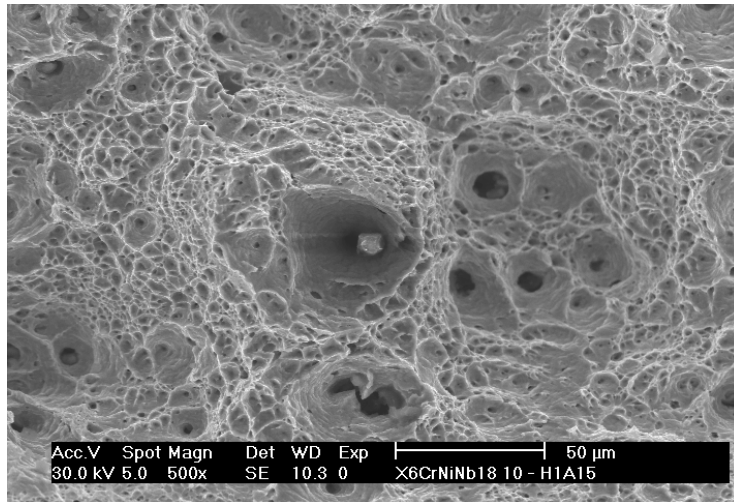
H1A15 ($\varnothing$ = 3 mm, $\acute{\varepsilon}$ = 10^{-1} s^{-1})
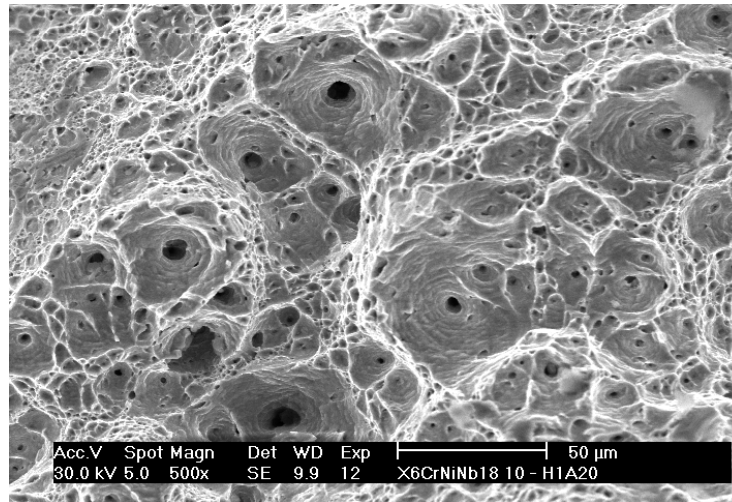
H1A20 ($\varnothing$ = 3 mm, $\acute{\varepsilon}$ = 200 s^{-1})

Fig. 10 : Dimple structures depending on the strain rates.
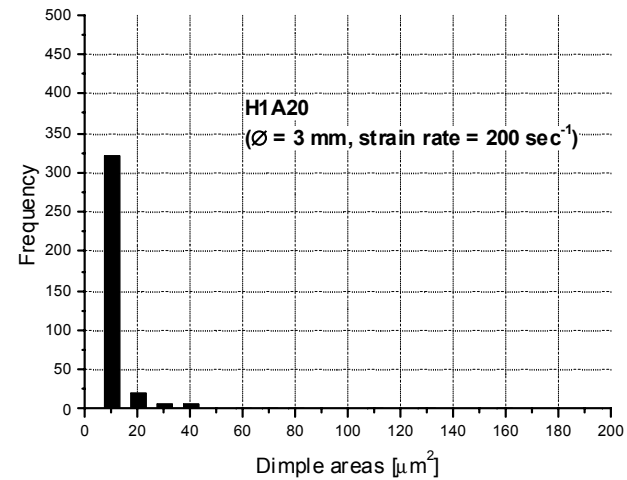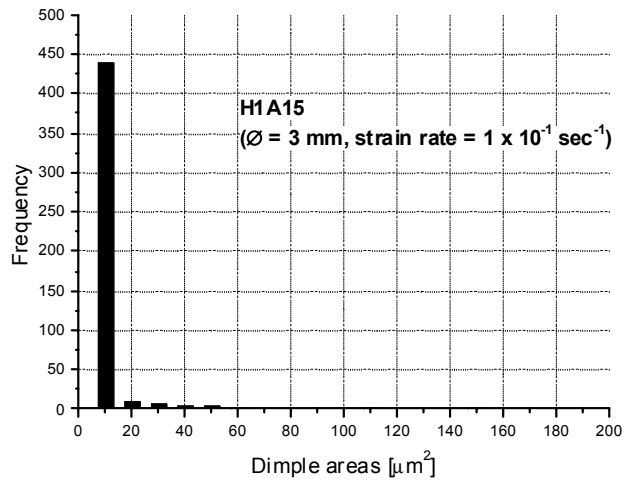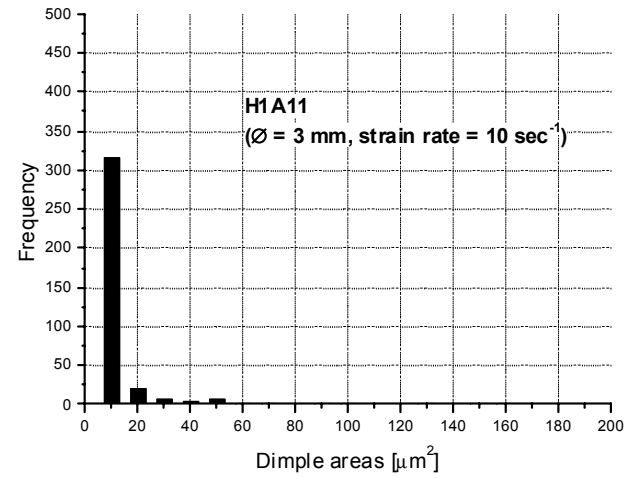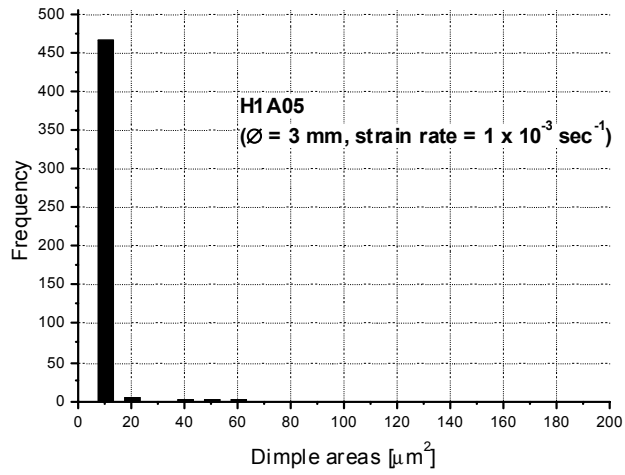
Fig. 11 : Dimple area distribution depending on the strain rates**.**
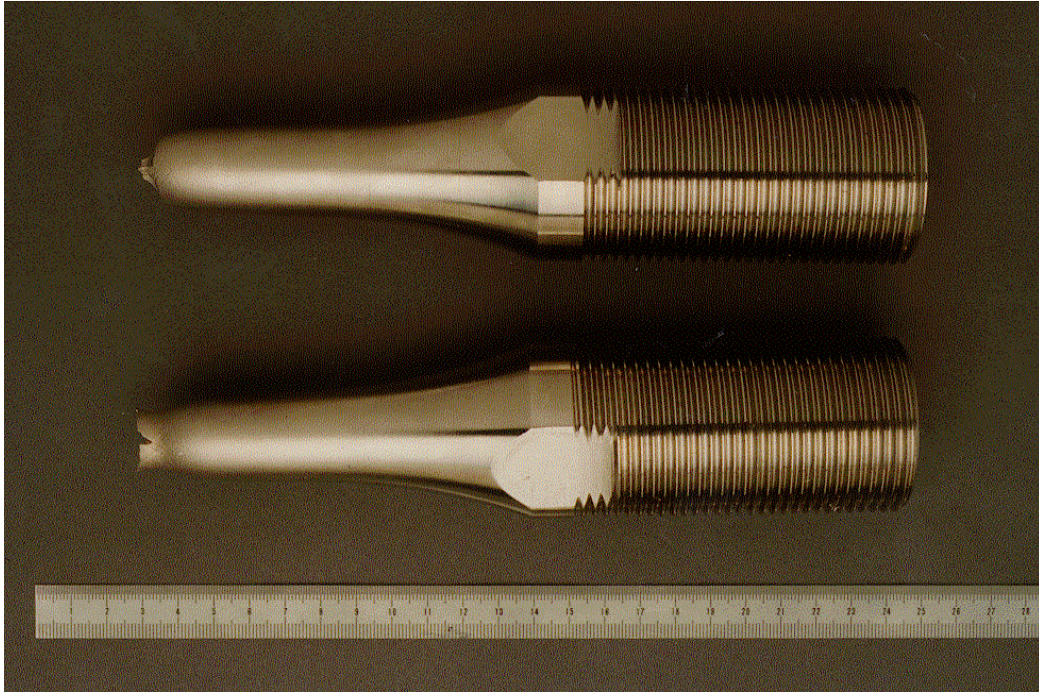
Fig. 12: Tensile sample H3A12, $\varnothing$ = 30 mm, strain rate = 150 s^{-1};
an overview.
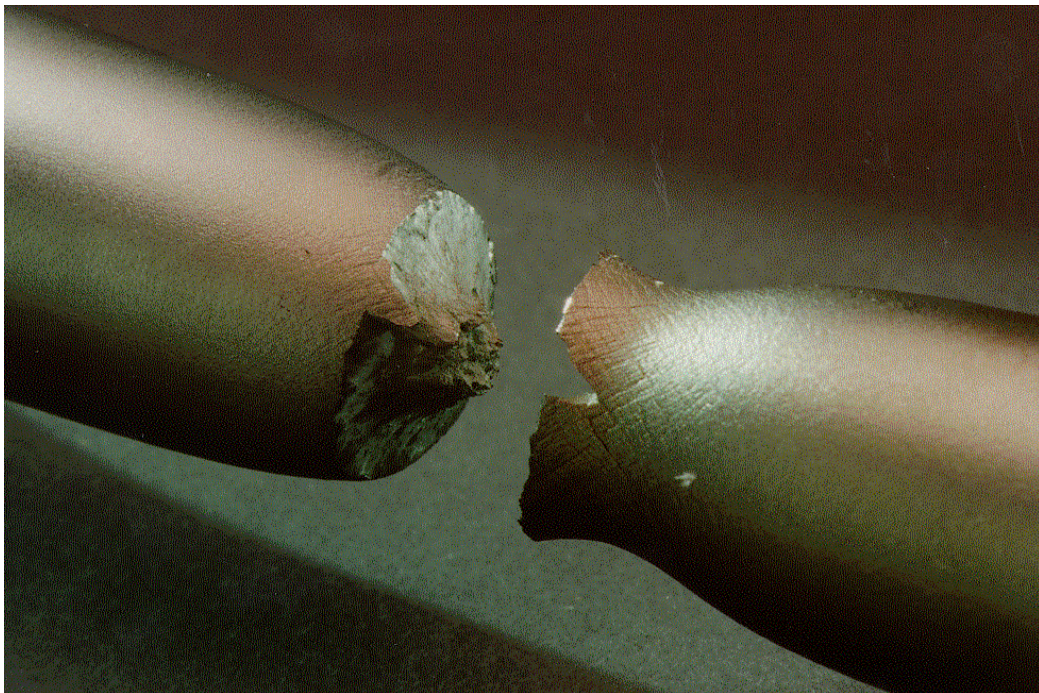
Fig. 13: Tensile sample H3A12, $\varnothing$ = 30 mm, strain rate = 150 s^{-1};
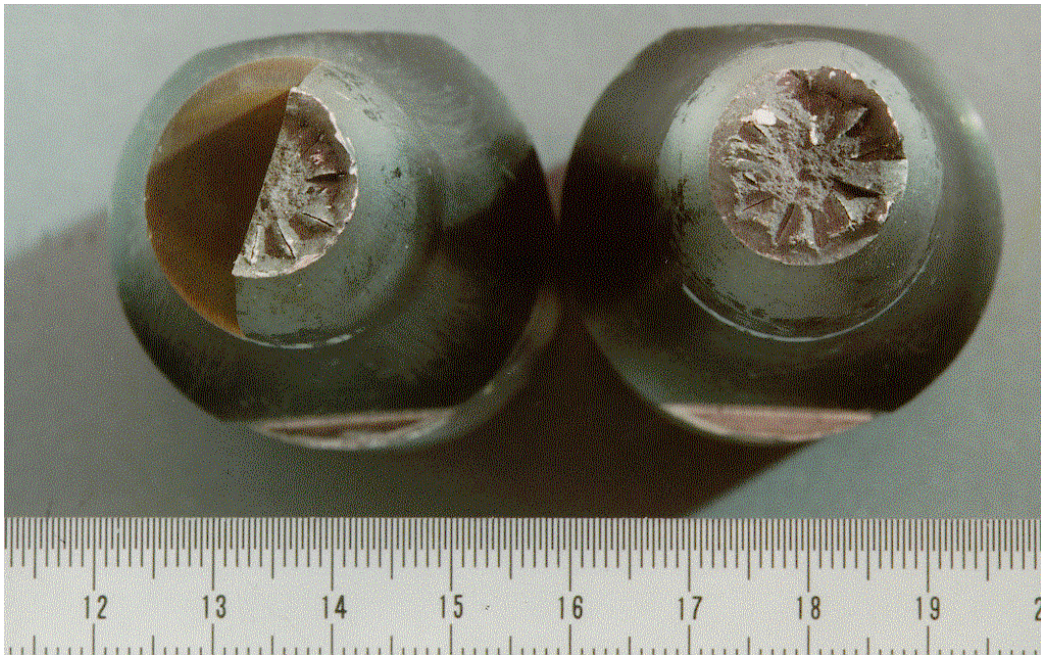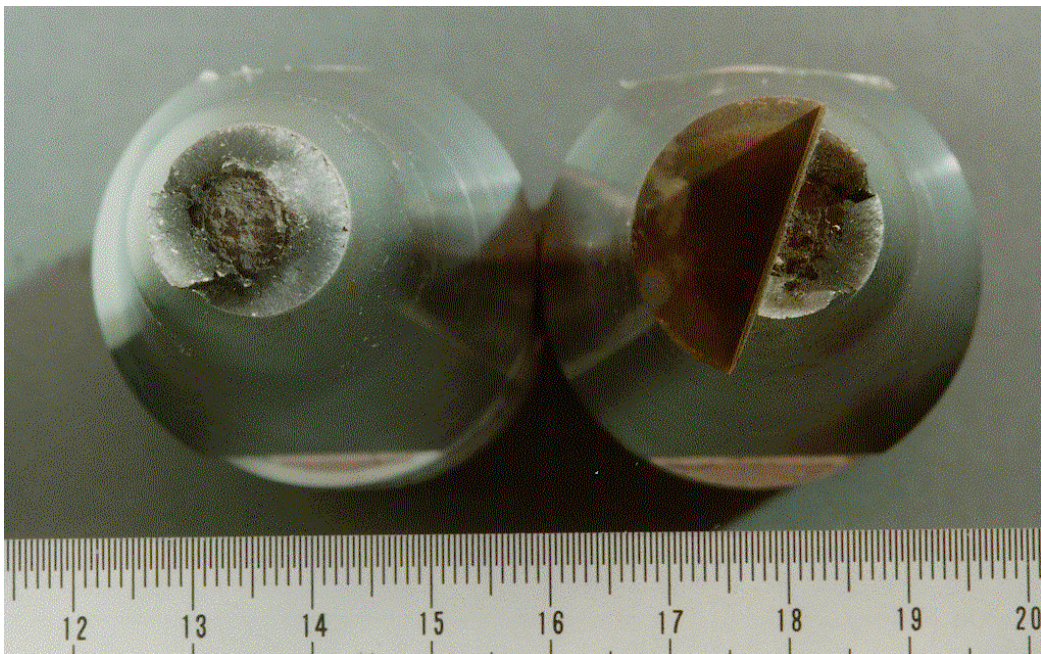the fracture area.
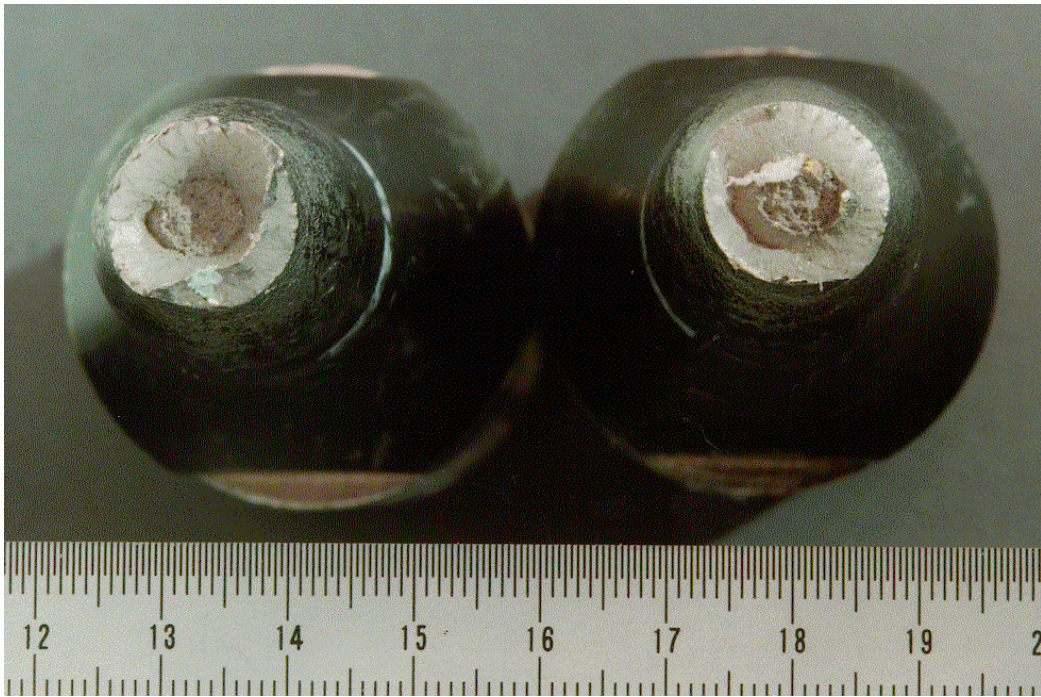
Fig. 14: Tensile sample H3A12, $\varnothing$ = 30 mm, strain rate = 1 x 10^{-3} s^{-1};
the fracture surfaces.
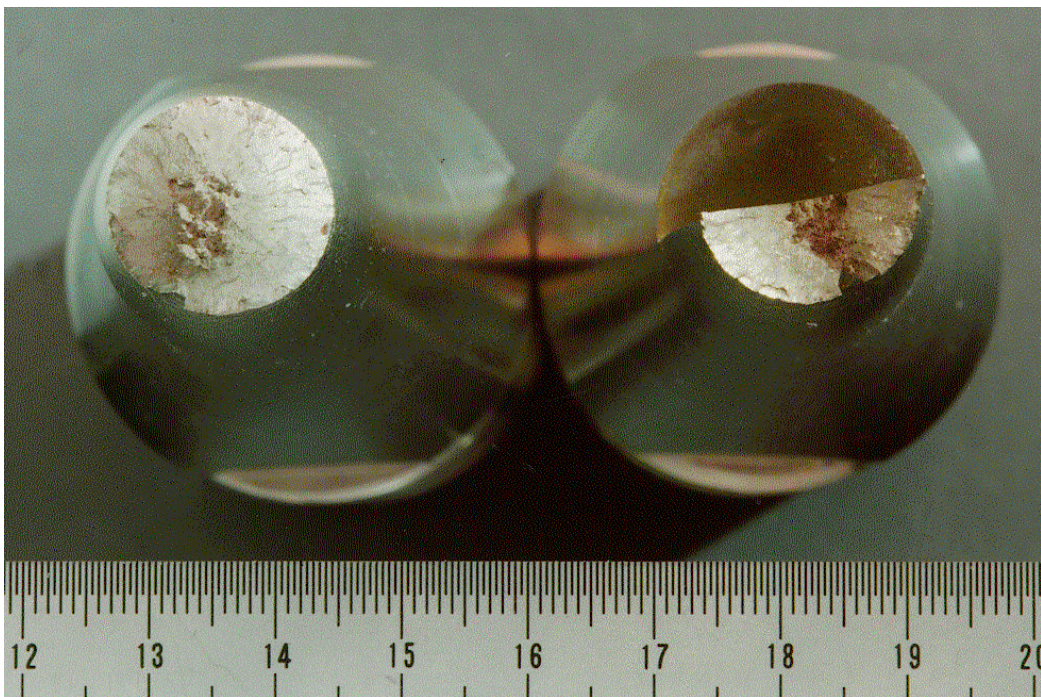
Fig. 15: Tensile sample H3A12, $\varnothing$ = 30 mm, strain rate = 150 s^{-1};
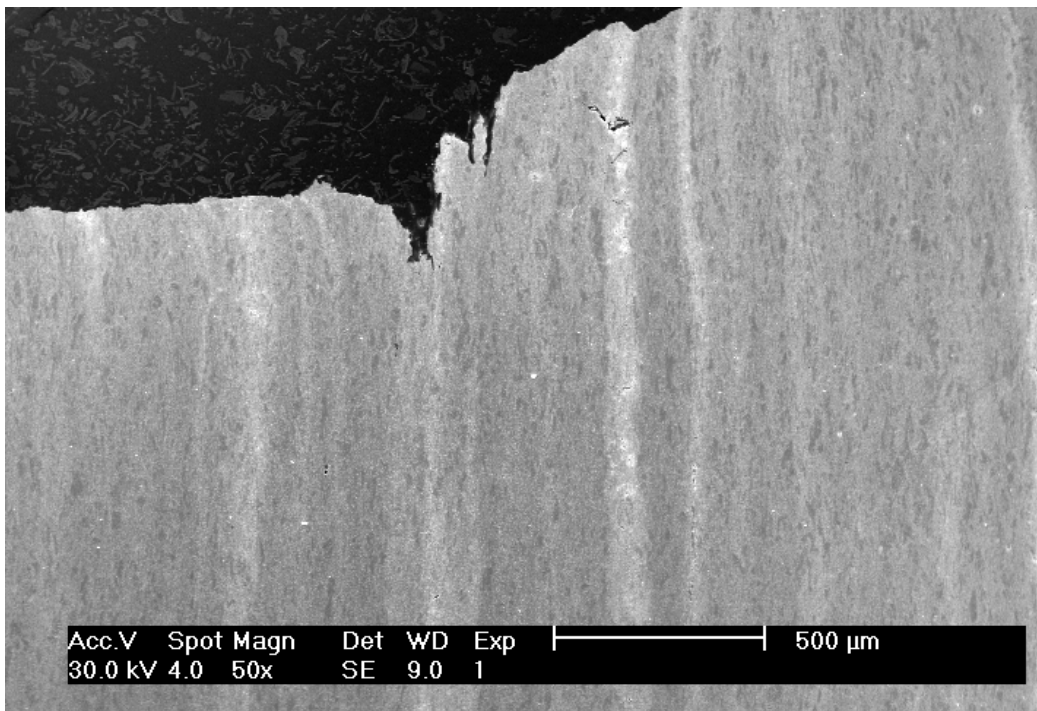the fracture surfaces.
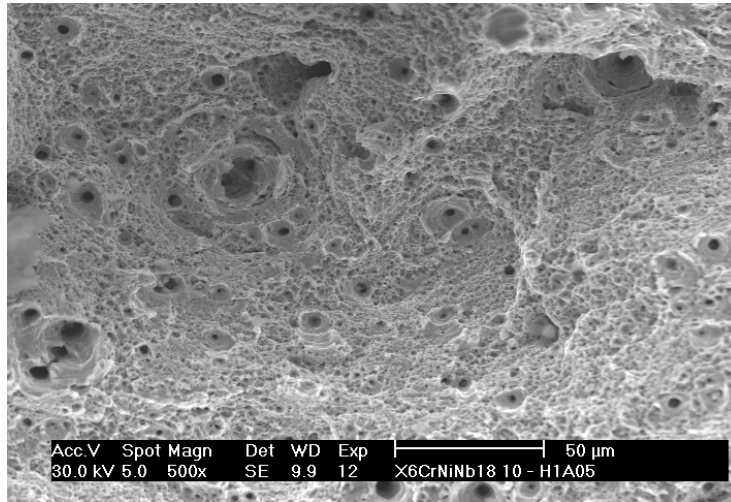
H1A05 ($\varnothing$ = 3 mm, $\acute{\epsilon}$ = 1 x 10^{-3} s^{-1})
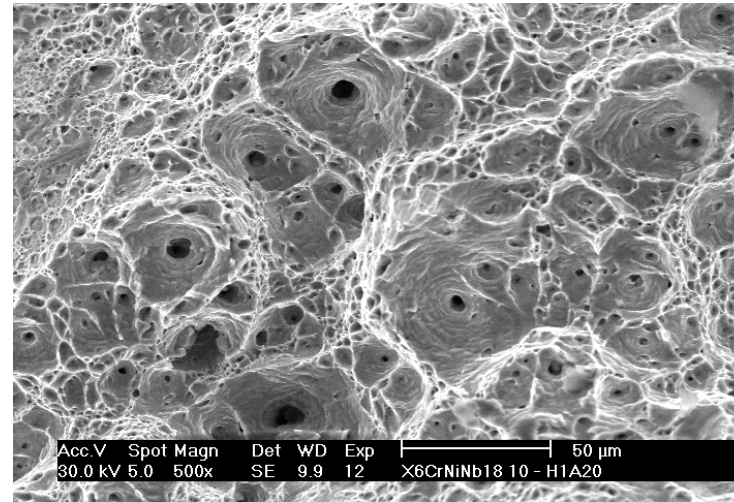
H1A20 ($\varnothing$ = 3 mm, $\acute{\epsilon}$ = 200 s^{-1})
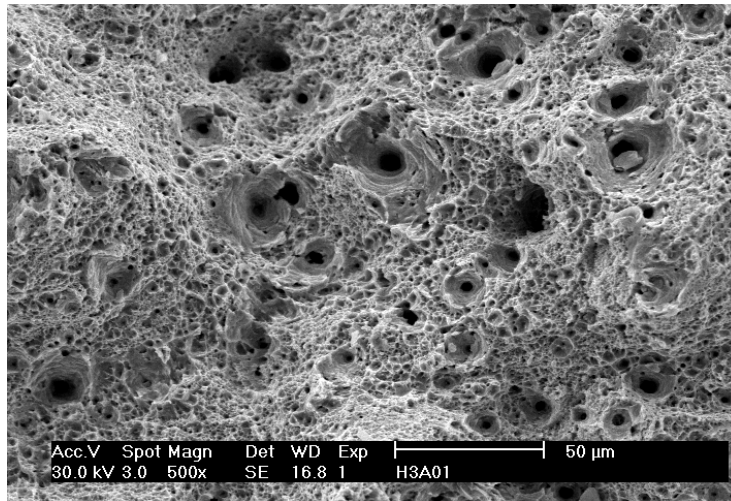
H3A01 ($\varnothing$ = 30 mm, $\acute{\epsilon}$ = 1 x 10^{-3} s^{-1})
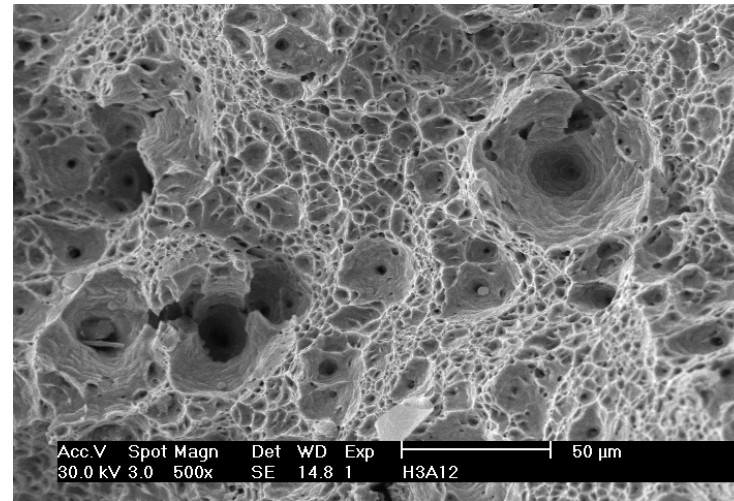
H3A12 ($\varnothing$ = 30 mm, $\acute{\epsilon}$ = 150 s^{-1})

Fig. 16: The dimple structures of different sample sizes, and tested at different strain rates.
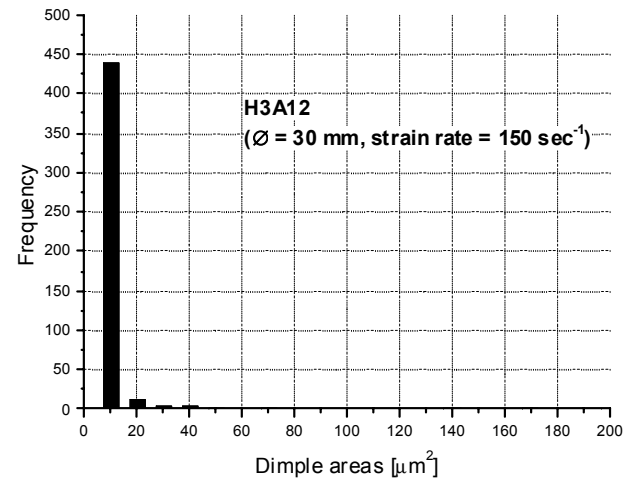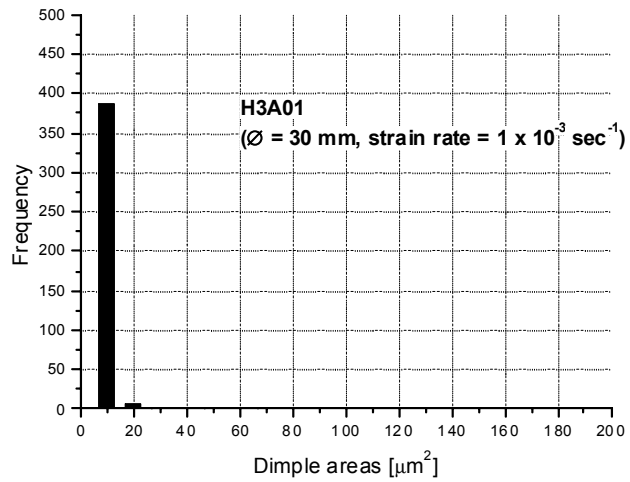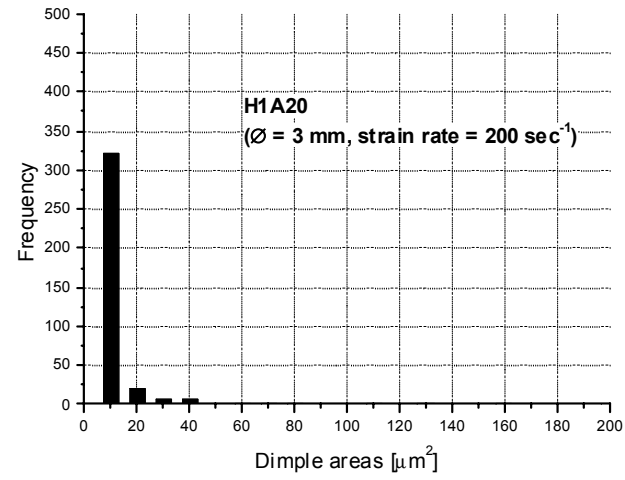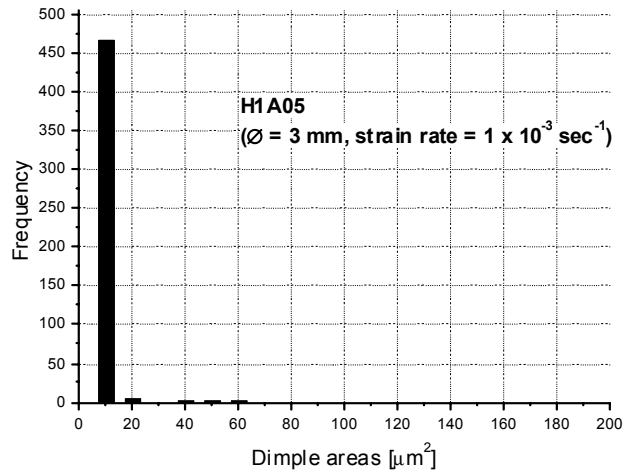
Fig. 17 : Dimple area distribution depending on the strain rates.
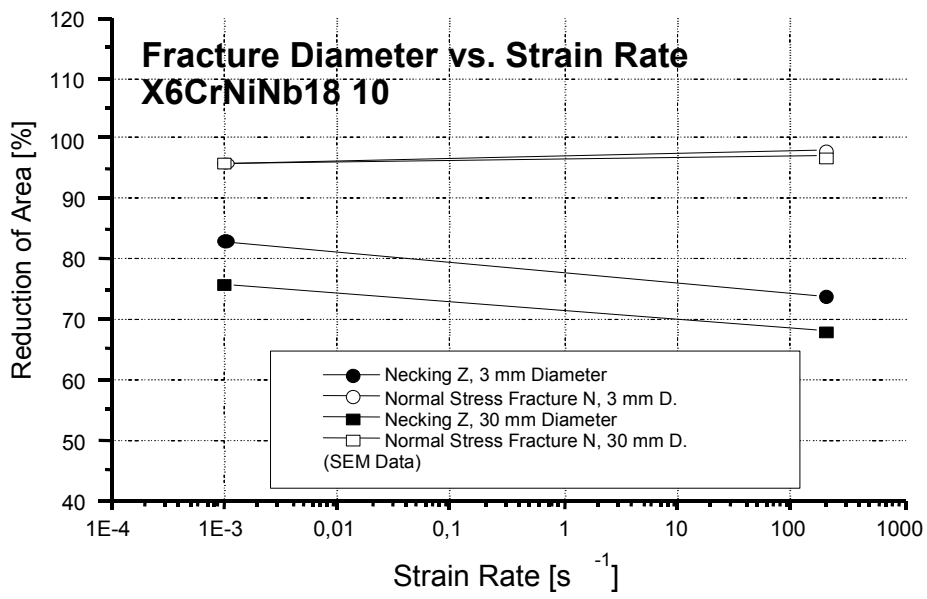
Fig. 18: Macroscopic fracture dimensions depending on the strain rates.
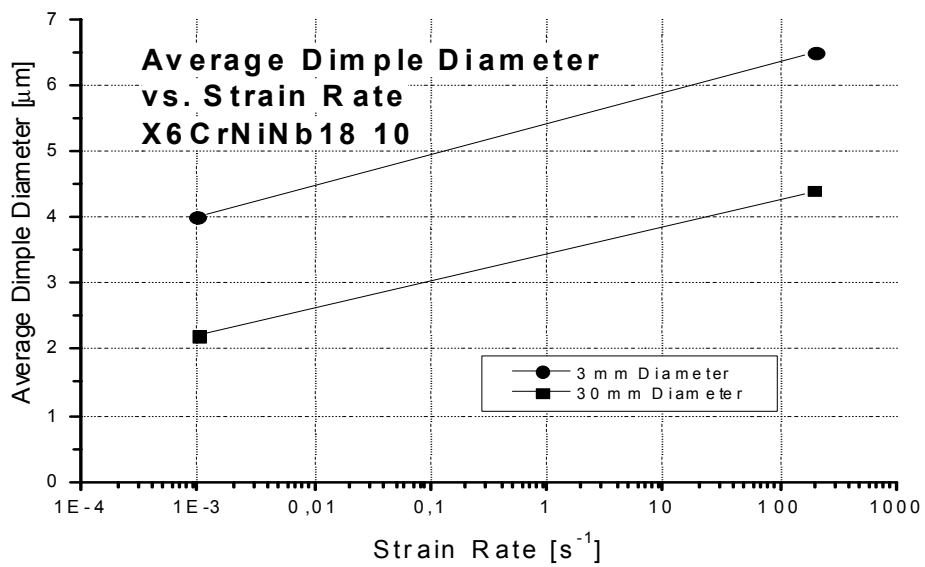
Fig. 19: Average dimple size depending on the strain rates.
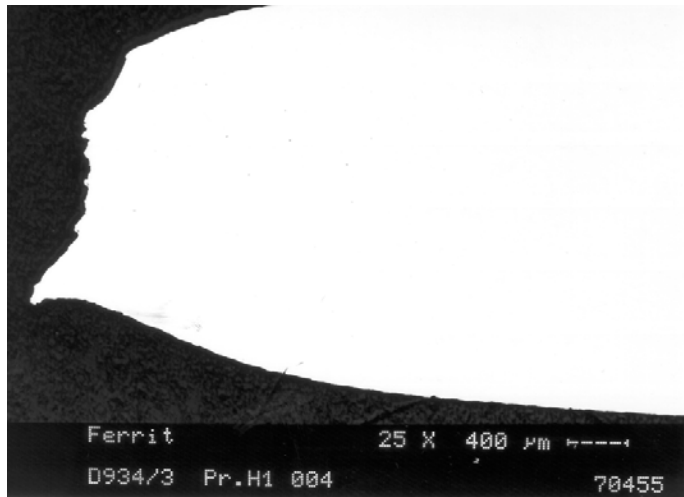
Middle length cut through the fracture (polished, 25x)
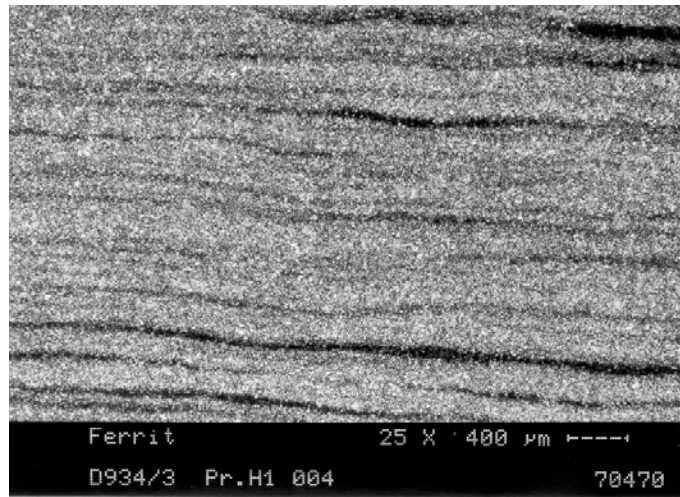
Grain formation in the sample head (etched, 25x)
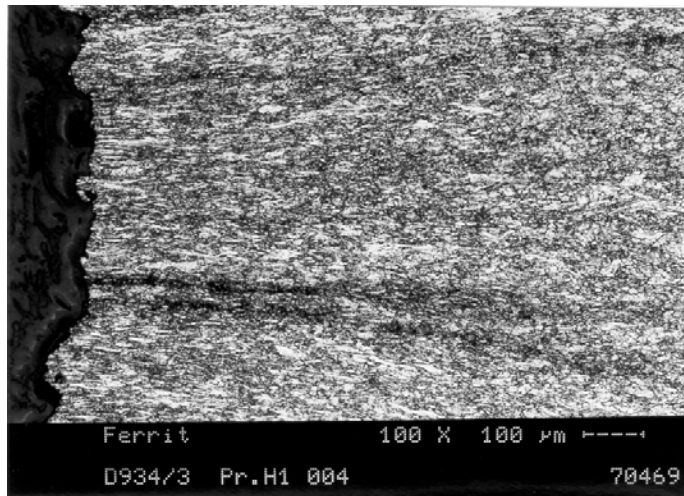
Grain formation of the fracture (etched, 100x)
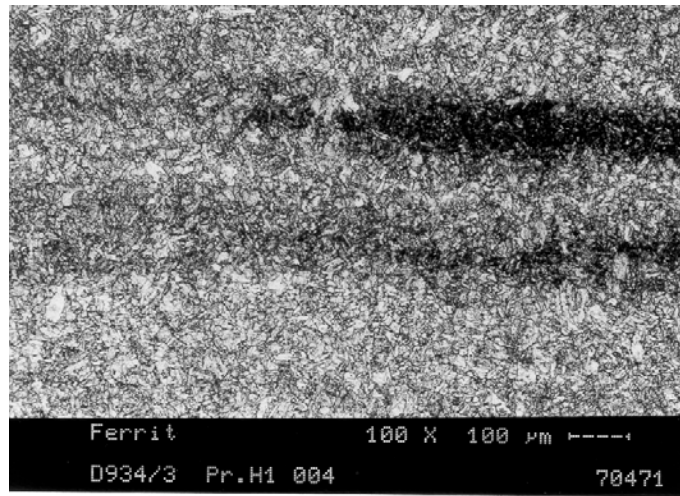
Grain formation in the sample head (etched, 100x)

Fig. 20: Metallographic cut of sample H1004.
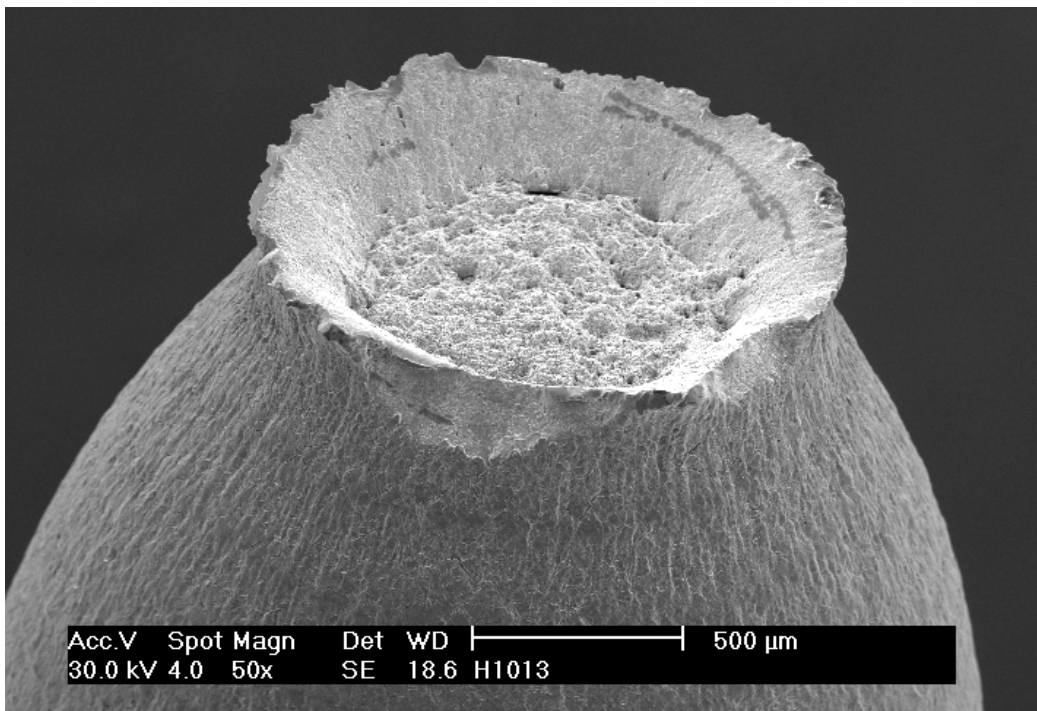
Fig. 21: Tensile sample H1013, $\varnothing$ = 3 mm, strain rate = 1 x 10^{-3} s^{-1}, the fracture surface.
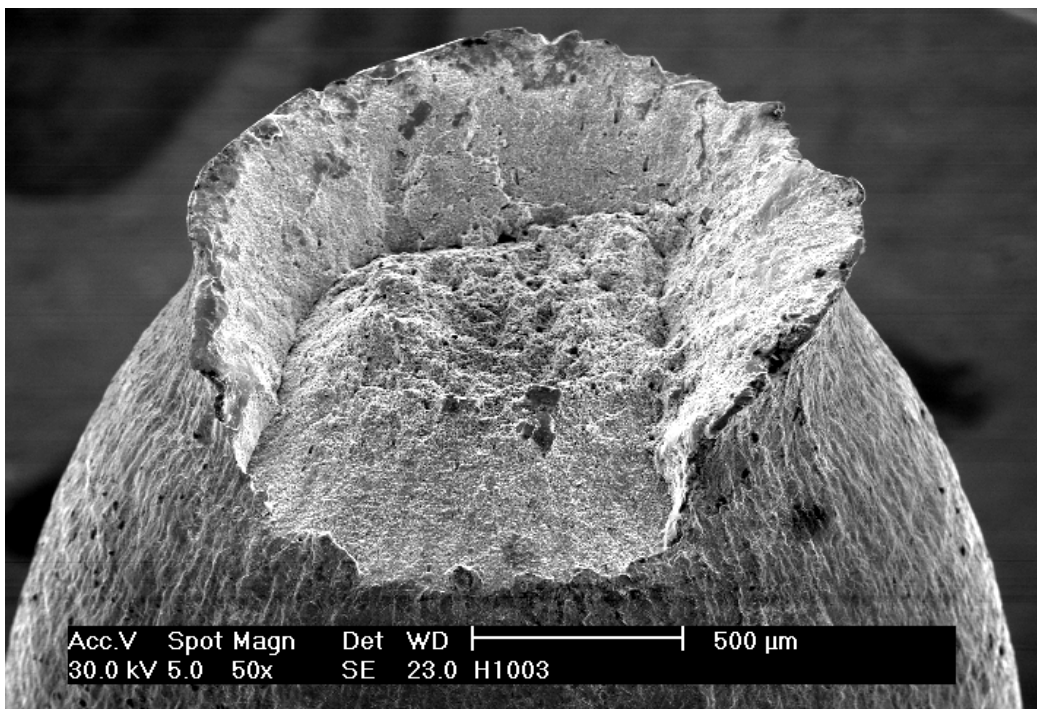
Fig. 22: Tensile sample H1003, $\varnothing$ = 3 mm, strain rate = 200 s^{-1}; the fracture surface.

Fig. 23: Tensile sample H3030, $\varnothing$ = 30 mm, strain rate = 1 x 10^{-3} s^{-1},
the fracture surfaces.

Fig. 24: Tensile sample H3001, $\varnothing$ = 30 mm, strain rate = 150 s^{-1};
the fracture surfaces.

Fig. 25: Tensile sample H3030, $\varnothing$ = 30 mm, strain rate = 1 x 10^{-3} s^{-1}, segregation bands near the fracture surface.
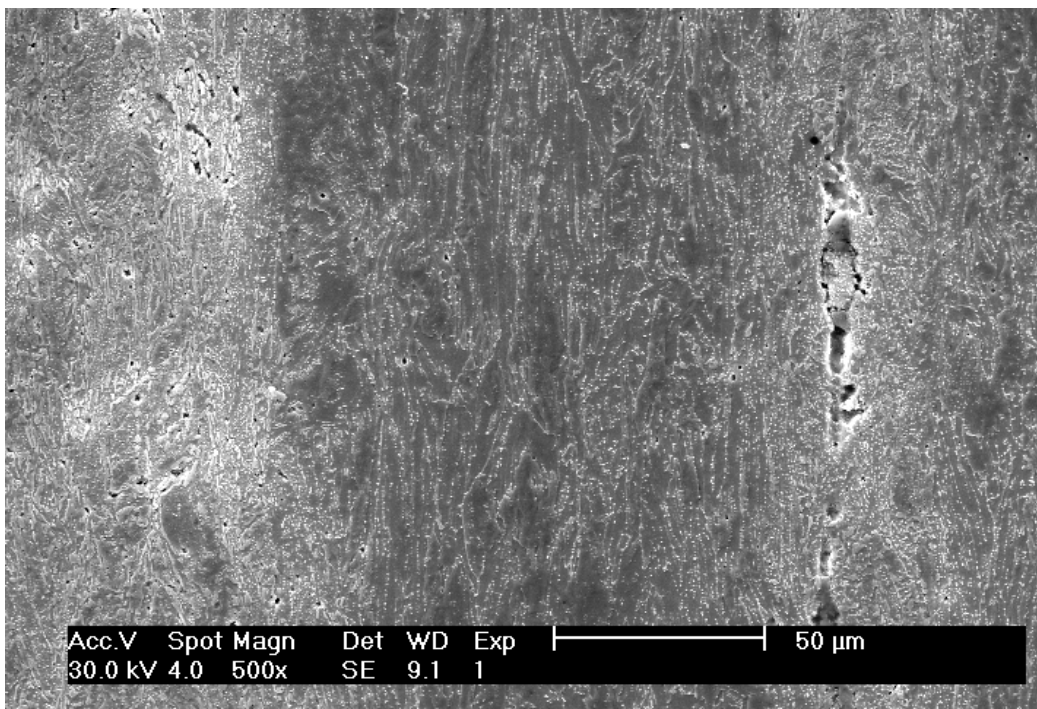
Fig. 26: Crack formations in the segregation bands (on the left) and cavities with MnS (on the right).
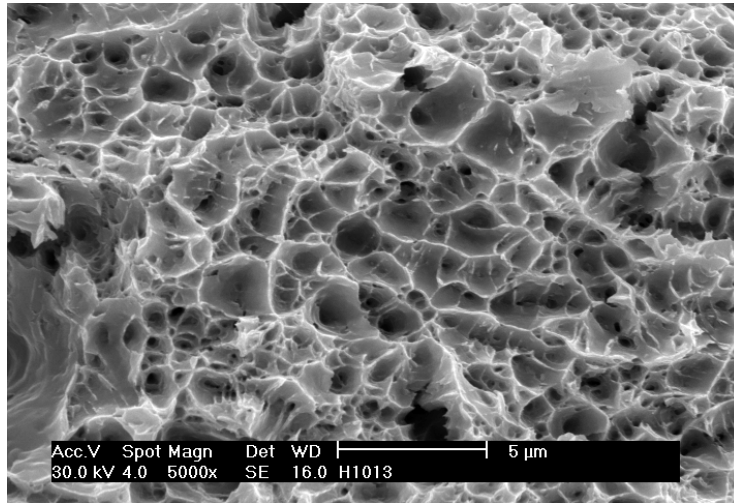
H1013 ($\varnothing$ = 3 mm, $\acute\varepsilon$ = 1 x 10^{-3} s^{-1})
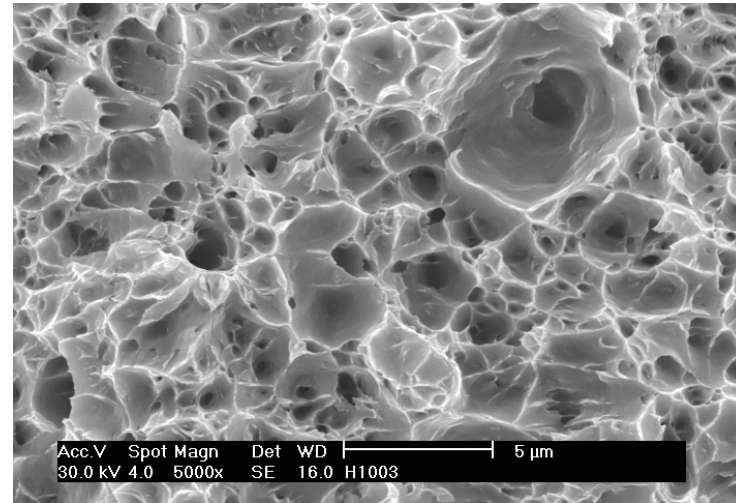
H1003 ($\varnothing$ = 3 mm, $\acute\varepsilon$ = 200 s^{-1})
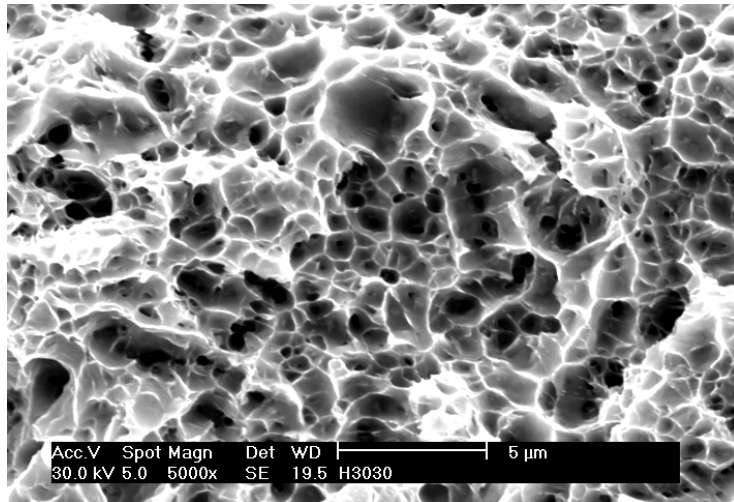
H3030 ($\varnothing$ = 30 mm, $\acute\varepsilon$ = 1 x 10^{-3} s^{-1})
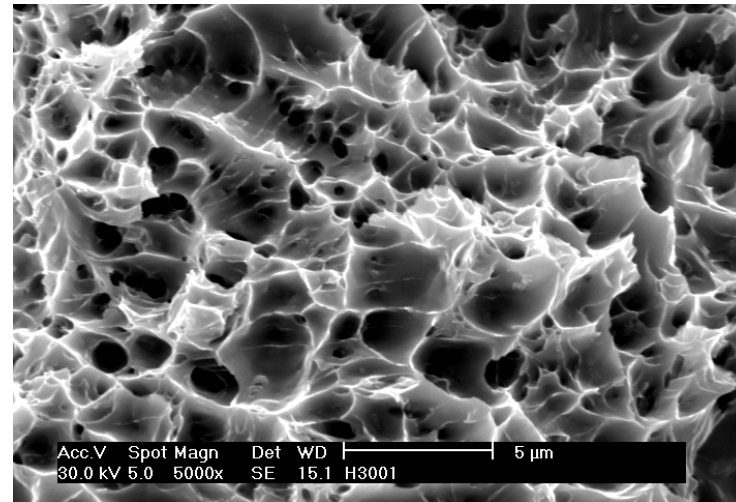
H3001 ($\varnothing$ = 30 mm, $\acute\varepsilon$ = 150 s^{-1})

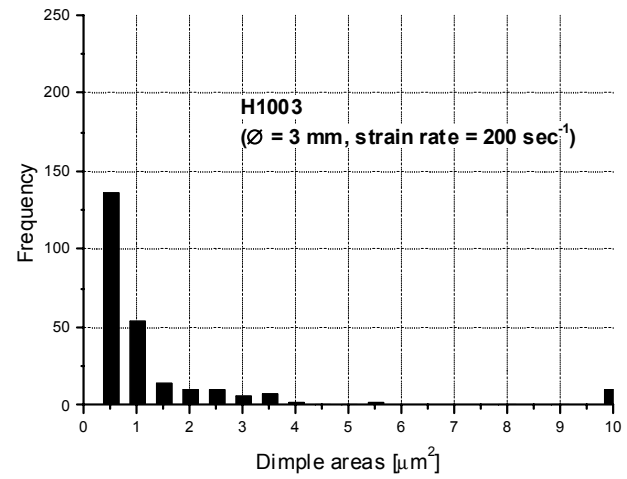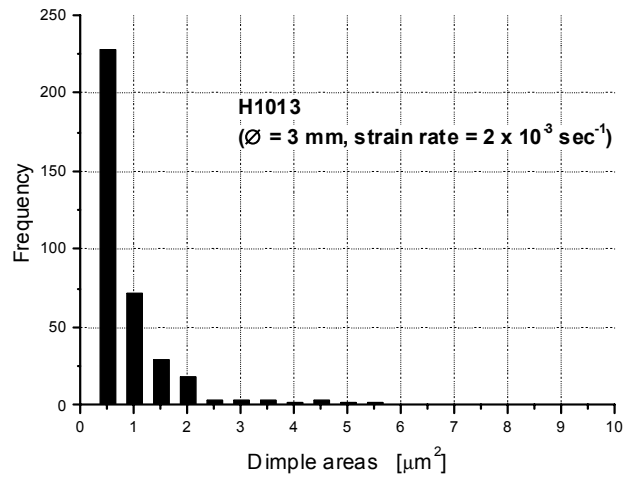**Fig. 27:** The dimple structures of different sample sizes, and tested at different strain rates.
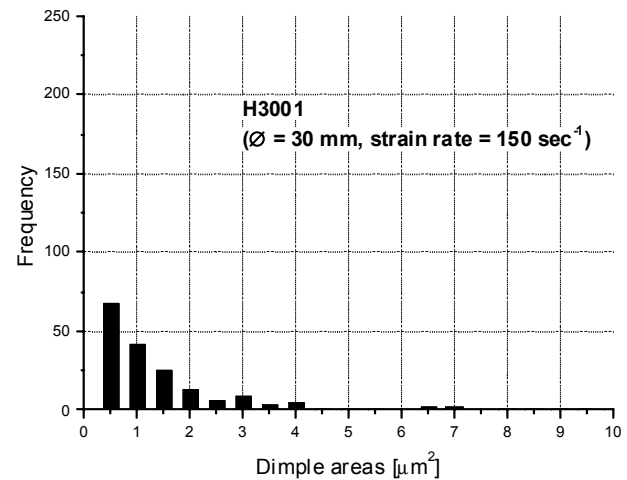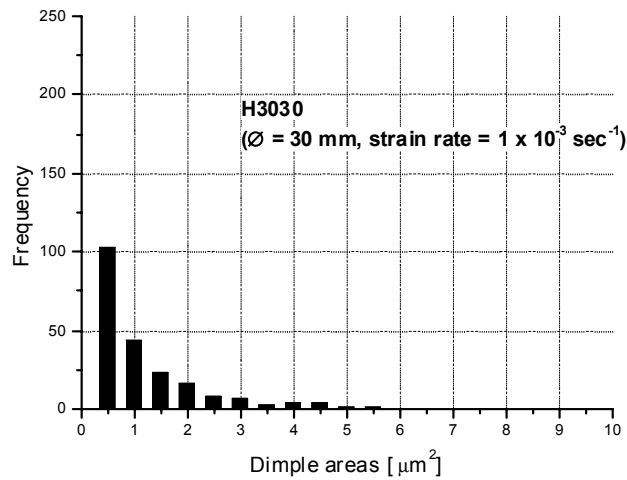
Fig. 28: Dimple area distribution depending on the strain rates**.**

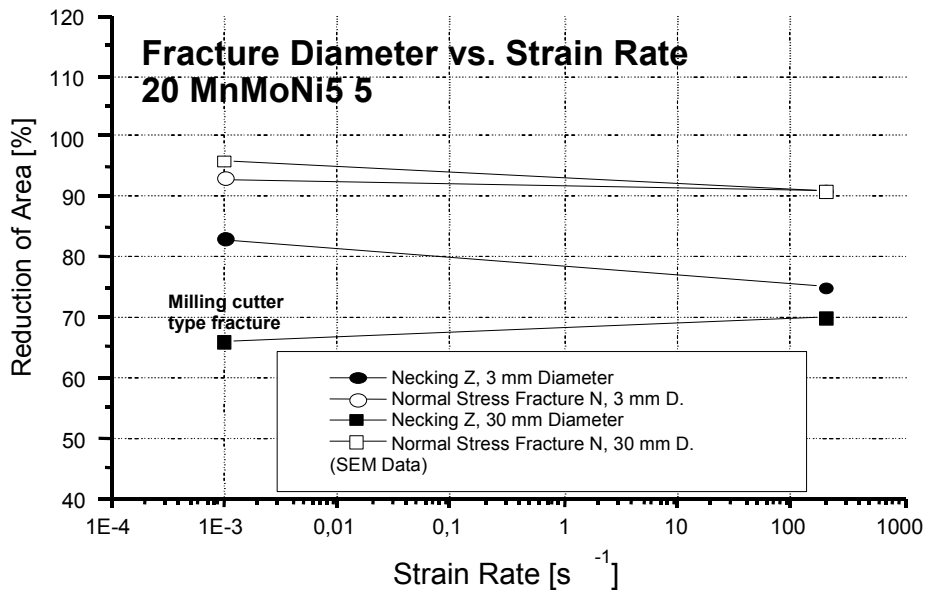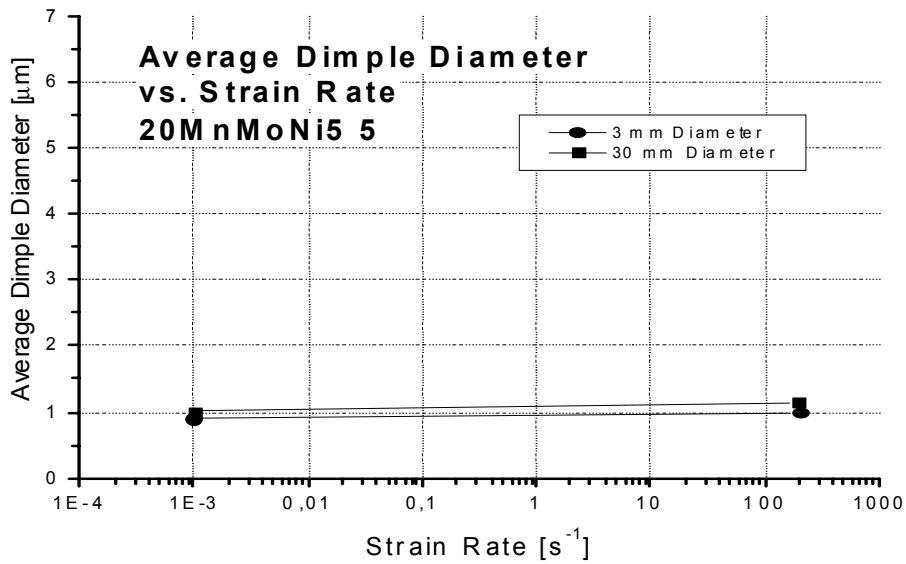**Fig. 29:** Macroscopic fracture dimensions depending on the strain rates.

Fig. 30: Average dimple size depending on the strain rates.